

# Routes to chaos in confined thermal convection arising from a cylindrical heat source

Diego Angeli<sup>1</sup>, Arturo Pagano<sup>2</sup>,  
Mauro A. Corticelli<sup>1</sup>, and Giovanni S. Barozzi<sup>1</sup>

<sup>1</sup> University of Modena and Reggio Emilia, Department of Mechanical and Civil Engineering, Via Vignolese, 905, I-41125 Modena, Italy  
(E-mail: [diego.angeli@unimore.it](mailto:diego.angeli@unimore.it))

<sup>2</sup> University of Catania, Department of Industrial and Mechanical Engineering Viale Andrea Doria, 6, I-95125 Catania, Italy  
(E-mail: [apagano@diim.unict.it](mailto:apagano@diim.unict.it))

**Abstract.** Natural convection flows arising from a horizontal cylinder centred in a square-sectioned enclosure are studied numerically. The sequence of bifurcations marking the transition of base fixed-point solutions to unsteady, chaotic flows is followed for increasing values of the Rayleigh number, and for two values of the enclosure aspect ratio,  $A$ . It is observed that, for the lower  $A$ -value, the route to chaos is triggered by a supercritical Hopf bifurcation, followed by a sequence of period-doublings, while, for the higher  $A$ -value, the symmetry of the system is broken by a pitchfork bifurcation, with periodic orbits originating from both branches, and eventually approaching chaos, exhibiting features typical of blue-sky catastrophes.

**Keywords:** Thermal convection, transition to chaos, bifurcations, period-doubling.

## 1 Introduction

Buoyancy-induced flows in enclosures are very complex in nature, and highly unpredictable, due to the bi-directional interaction between the flow and temperature fields, and the sensitivity of the thermal-flow regimes to the geometric and thermal configuration of the system.

The importance of bifurcations and chaos in buoyancy-induced flows as a research topic goes far beyond the field of thermal sciences. In fact, it is deeply entwined with the history of chaos theory, since the discovery of the renowned Lorenz attractor, originating from a simplified Rayleigh-Bénard convection model [1]. From that seminal study, many works have been carried out on the non-linear dynamics of thermal convection in basic enclosure configurations, such as the rectangular enclosures heated from below and from the side [2,3], and, more recently, the horizontal annulus between two coaxial cylinders [4]. Fewer works dealt with more complex geometrical and thermal configurations [5,6]. Nevertheless, from a theoretical and practical standpoint, the interest in this topic is growing continuously.

The physical system considered in the present study is the cavity formed by an infinite square parallelepiped with a centrally placed cylindrical heating source. The system is approximated to its 2D transversal square section containing a circular heat source, as sketched in Fig. 1. The temperature of both enclosure and cylinder is assumed as uniform, the cylindrical surface being hotter than the cavity walls. The resulting flow is investigated with respect to the leading parameter of the non-dimensionalized problem, the Rayleigh number  $Ra$ , based on the gap width  $H$ , and for two values of the aspect ratio  $A = L/H$ , between the cavity side length and the minimum enclosure to cylinder gap width, namely  $A = 2.5$  and  $A = 5$ . The third parameter of the system, the Prandtl number, is fixed at a value  $Pr = 0.7$ , representative of air at environmental conditions.

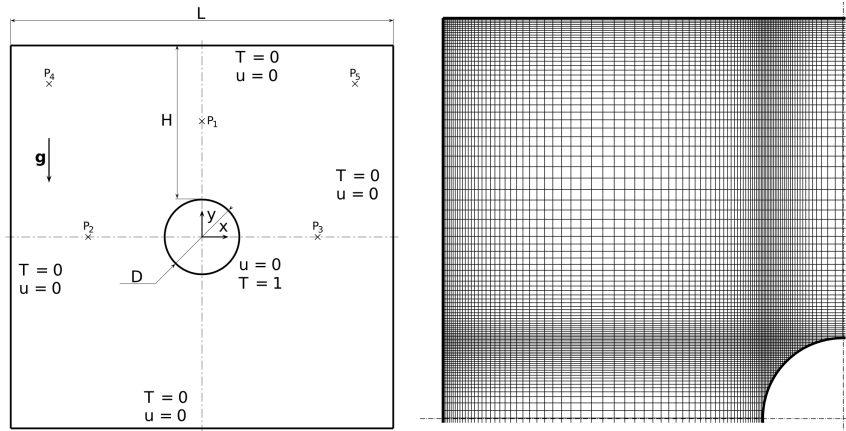


**Fig. 1.** Left: schematic of the system under consideration; ( $\times$ ) symbols indicate locations of the sampling points. Right: quadrant of the computational grid for  $A = 2.5$ .

Numerical predictions are carried out by means of a specifically developed finite-volume code. Successive bifurcations of the low- $Ra$  fixed point solution are followed for increasing  $Ra$ . To this aim, time series of the dependent variables (velocity components and temperature), are extracted in 5 locations represented in Fig. 1 by points P1 to P5. Nonlinear dynamical features are described by means of phase-space representations, power spectra of the computed time series, and of Poincaré maps.

## 2 Numerical method

The problem is stated in terms of the incompressible Navier-Stokes formulation, under the Boussinesq approximation. The governing equations (continuity, momentum and energy) are tackled in their non-dimensional form:

$$\nabla \cdot \mathbf{u} = \mathbf{0} \quad (1)$$

$$\frac{\partial \mathbf{u}}{\partial t} + \mathbf{u} \cdot \nabla \mathbf{u} = -\nabla p + \frac{Pr^{1/2}}{Ra^{1/2}} \nabla^2 \mathbf{u} + T \hat{\mathbf{g}} \quad (2)$$

$$\frac{\partial T}{\partial t} + \mathbf{u} \cdot \nabla T = \frac{1}{(RaPr)^{1/2}} \nabla^2 T \quad (3)$$

where  $t$ ,  $\mathbf{u}$ ,  $p$  and  $T$  represent the dimensionless time, velocity vector, pressure and temperature, respectively, and  $\hat{\mathbf{g}}$  is the gravity unit vector. A value  $Pr = 0.7$  is assumed for air. Boundary conditions for  $T$  and  $\mathbf{u}$  are reported in Figure 1.

The numerical technique adopted is based on a second-order, Finite Volume implementation of equations (1)-(3) on non-uniform Cartesian grids: a more detailed description of the spatial and temporal discretization schemes is found in [7]. The 2D modelling of arbitrarily irregular boundaries on Cartesian grids is achieved thanks to the original scheme developed by Barozzi *et al.* [8], which preserves second-order accuracy for the method, as well as the computational efficiency of the Cartesian approach.

In view of the work objectives, special care was put on the grid sizing of both near-wall areas and internal domain regions, as shown in Fig. 1. The average cell spacing in each region was chosen according to scaling considerations, as illustrated in [6]. The time step size has been chosen small enough so as to ensure a suitably accurate reproduction of the continuous-time system dynamics.

For either  $A$ -value, the initial conditions were chosen so as to follow the evolution of low- $Ra$  base-flow, fixed-point solutions [7]. In order to detect the occurrence of successive bifurcations,  $Ra$  was increased monotonically with suitable steps, each simulation starting from the final frame of the preceding one. All the simulations were protracted to steady-state or, when unsteady flows were detected, until a fixed dimensionless time span was covered.

$A = 2.5$ ( $190 \times 190$ grid)		$A = 5$ ( $288 \times 288$ grid)	
$Ra$	Bifurcation	$Ra$	Bifurcation
$4 \times 10^4$	$S$ (base flow)	$1.8 \times 10^4$	$S$ (base flow)
$6.6 \sim 6.8 \times 10^4$	$S \rightarrow P_1$ (supercritical Hopf)	$3.2 \sim 3.4 \times 10^4$	$S \rightarrow NS$ (pitchfork)
$1.7 \sim 1.8 \times 10^5$	$P_1 \rightarrow P_2$ (period-doubling)	$6.0 \sim 7.0 \times 10^4$	$NS \rightarrow P$ (Hopf)
$1.8 \sim 1.9 \times 10^5$	$P_2 \rightarrow P_4$ (period-doubling)	$6.0 \sim 7.0 \times 10^5$	$P \rightarrow N$ (Blue-sky catastrophe)
$1.9 \sim 2.0 \times 10^5$	$P_4 \rightarrow \dots \rightarrow N$		

**Table 1.** Bifurcations of the low- $Ra$  base flow solution for each  $A$ .

### 3 Results and discussion

Table 2 summarizes the sequences of bifurcations leading to chaos for both values of the aspect ratio  $A$ . The nomenclature used in defining the different types of asymptotic behaviours follows the systematic introduced by Angeli *et al.* [4]. In the following, details of both routes are briefly illustrated by means of established nonlinear analysis tools.

For  $A = 2.5$ , starting from the base solution at  $Ra = 4 \cdot 10^4$ , the system asymptotically reaches a fixed-point for  $Ra \leq 6.6 \times 10^4$ . As  $Ra$  is increased from  $Ra = 6.6 \times 10^4$  to  $Ra = 6.8 \times 10^4$ , oscillatory behaviour sets in, until a periodic limit cycle is reached. In Fig. 2, 2D projections of the corresponding  $T$ - $u_x$ - $u_y$  attractors are plotted as a function of  $Ra$ . The passage from the lower- $Ra$  fixed-point solution to the periodic orbit is clearly portrayed, thus suggesting the occurrence of a Supercritical Hopf bifurcation.

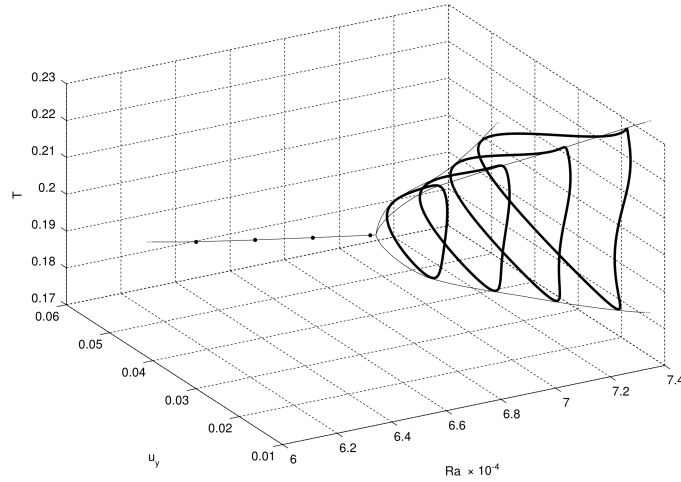


**Fig. 2.** Sequence of 2D attractors  $u_y$ - $T$  at point P2, for  $A = 2.5$  and for increasing  $Ra$ .

Fig. 3 reports the power spectral density distribution of the temperature time series at point P1 for the case  $A = 2.5$  and for increasing values of the Rayleigh number. The values of  $Ra$  have been chosen with the aim of showing the occurrence of a period doubling route to chaos which characterises the evolution of the system dynamics for the mentioned aspect ratio. In fact, it is possible to observe that the two original fundamental harmonics observed in the power spectrum of temperature at  $Ra = 1.7 \times 10^5$  become four for  $Ra = 1.8 \times 10^5$  and double again for  $Ra = 1.9 \times 10^5$ ; the last case, at  $Ra = 2.0 \times 10^5$ , is instead characterised by a broadband power spectrum, which represents a first hint of chaotic dynamics, with the broadened bands arising around the original harmonics of the previous cases.

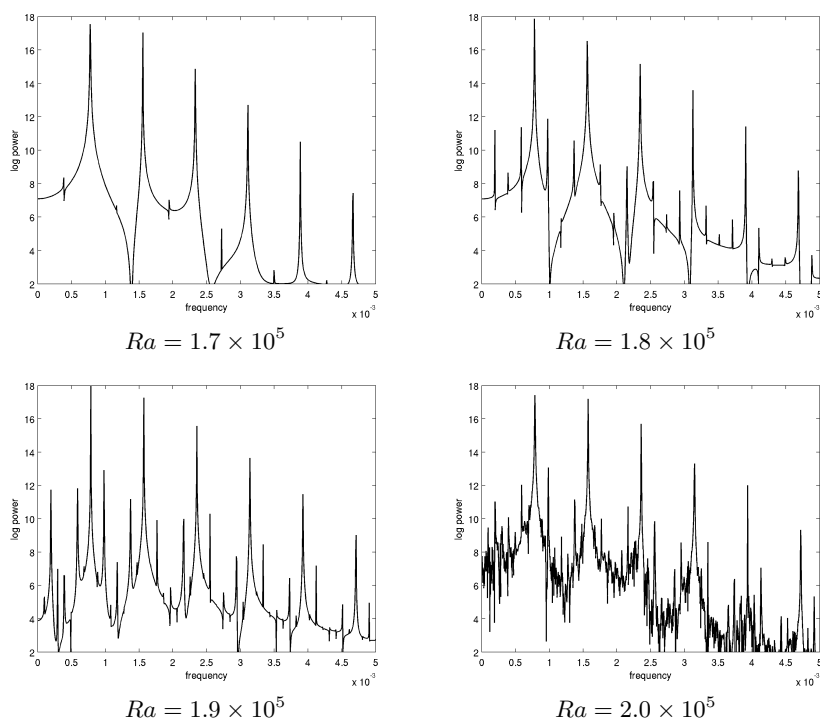


**Fig. 3.** Power spectral density of  $T$  at point P1, for  $A = 2.5$  and for increasing  $Ra$

This observation is confirmed by the analysis of the system attractors reported in the  $T-u_x-u_y$  state space, as reported in Fig. 4. Considering that each of the fundamental harmonics observed in the power spectrum corresponds to a loop of the attractor in the phase space representation, it is possible to observe that the original two-loop limit cycle at  $Ra = 1.7 \times 10^5$  gives rise to a four-loop limit cycle at  $Ra = 1.8 \times 10^5$ , which, in turn, is doubled again in an eight-loop limit cycle at  $Ra = 1.9 \times 10^5$ . Finally, for the last of the reported values of  $Ra$ ,  $Ra = 2.0 \times 10^5$ , in accordance with previous observations on the power spectrum, the attractor shows a chaotic morphology, with fractal bands distributed around the loops of the original limit cycles.

Fig. 4 reports also the intersections of the 3-dimensional attractors with Poincaré surfaces of section that have been obtained considering the plane  $u_x-T$  passing by the mean values of the calculated time series of the state variable  $u_y$ . Such intersections have been reported in the maps in Fig. 5. It is observed that a couple of intersections arises for each loop of the limit cycle. Again, the successive period doublings can be observed by spanning the maps at  $Ra = 1.7 \times 10^5$  to  $Ra = 1.8 \times 10^5$  and, then, to  $Ra = 1.9 \times 10^5$ , whereas ordered series of intersections, typical of deterministic chaotic dynamics, characterise the Poincaré map at  $Ra = 2.0 \times 10^5$ . For brevity, it is just mentioned here that an accurate observation of the local structure of such series of intersections reveals the stretching and folding typical of fractal sets.

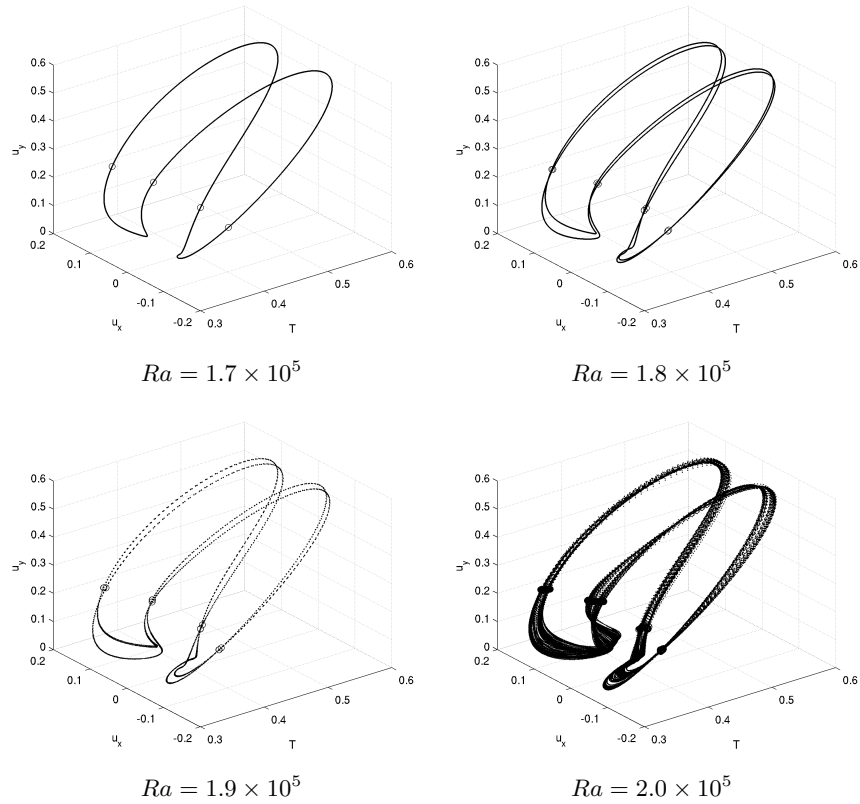


**Fig. 4.** 3D attractor in state space  $T$ - $u_x$ - $u_y$  at point P1, for  $A = 2.5$  and for increasing  $Ra$

For the higher value of the aspect ratio  $A$  considered,  $A = 5$ , the system undergoes a different sequence of bifurcations leading to chaos. Fig. 6(a) represents the evolution of the  $T$ - $u_y$  attractors at point P2 as a function of  $Ra$ . As  $Ra$  is increased beyond  $Ra = 3.2 \times 10^4$ , the base flow becomes unstable, and gives rise to two different solution branches, suggesting the occurrence of a pitchfork bifurcation (whose sub- or supercritical nature is still to be ascertained). The two solution branches correspond to stable mirrored dual solutions [6].

By further increasing  $Ra$ , each of the two solution branches undergo a Hopf bifurcation to a periodic limit cycle, as clearly visible in Fig. 6(a). Such transition occurs between  $Ra = 6 \times 10^4$  and  $Ra = 7 \times 10^4$ . The periodic orbits remain stable for a wide range of  $Ra$ -values, up to  $Ra = 6 \times 10^5$ . From Fig. 6(b), a progressive increase of the period of the limit cycle, *i.e.* of the loop extension can be appreciated. This trend eventually leads to the chaotic attractor reported in Fig. 6(c), for  $Ra = 7 \times 10^5$ , in a general evolution which seems to belong to the class of blue-sky catastrophes [9]. Such an observation deserves further analyses which, however, are beyond the scope of the present study.

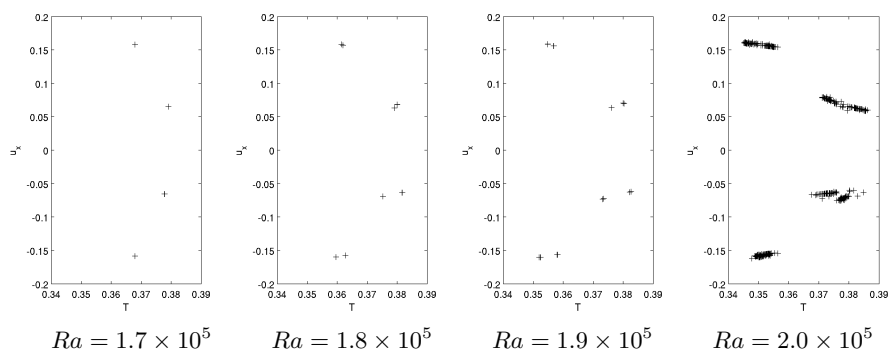


**Fig. 5.** Poincaré surfaces of section of the 3D attractors at point P1, for  $A = 2.5$  and for increasing  $Ra$

#### 4 Concluding remarks

Natural convection flows arising from a horizontal cylindrical source centred in a square enclosure were investigated numerically. Two values of the aspect ratio  $A$  were considered; for which the entire scenario leading to deterministic chaos was outlined, for increasing values of the Rayleigh number.

For the lower  $A$ -value,  $A = 2.5$ , the flow undergoes a Hopf bifurcation, followed by a sequence of period-doublings. For the higher  $A$ -value,  $A = 5$ , a pitchfork bifurcation gives rise to stable periodic orbits, persisting for a large range of  $Ra$ -values. Chaotic behaviour is finally observed, on top of an evolution which resembles a blue-sky catastrophe.

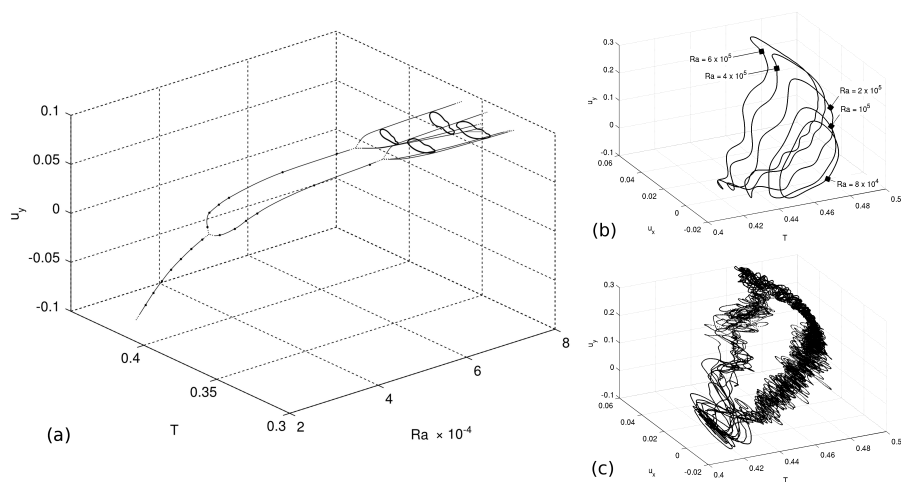


**Fig. 6.** (a) Sequence of 2D attractors  $T-u_y$  at point P2, for  $A = 5$  and for increasing  $Ra$ ; (b) 3D periodic orbits in state space  $T-u_x-u_y$  at point P1, for  $A = 5$  and for increasing  $Ra$ ; (c) chaotic attractor at point P1, for  $A = 5$  and  $Ra = 7 \times 10^5$ .

## References

- 1.E. N. Lorenz. Deterministic nonperiodic flow. *Journal of Atmospheric Sciences*, 20:130–141, 1963.
- 2.K. T. Yang. Transitions and bifurcations in laminar buoyant flows in confined enclosures. *ASME Journal of Heat Transfer*, 110:1191–1204, 1988.
- 3.P. Le Quéré. Onset of unsteadiness, routes to chaos and simulations of chaotic flows in cavities heated from the side: a review of present status. In G. F. Hewitt, editor, *Proceedings of the Tenth International Heat Transfer Conference*, volume 1, pages 281–296, Brighton, UK, 1994. Hemisphere Publishing Corporation.
- 4.D. Angeli, G. S. Barozzi, M. W. Collins, and O. M. Kamiyo. A critical review of buoyancy-induced flow transitions in horizontal annuli. *International Journal of Thermal Sciences*, 49:2231–2492, 2010.
- 5.G. Desrayaud and G. Lauriat. Unsteady confined buoyant plumes. *Journal of Fluid Mechanics*, 252:617–646, 1998.
- 6.D. Angeli, A. Pagano, M. A. Corticelli, A. Fichera, and G. S. Barozzi. Bifurcations of natural convection flows from an enclosed cylindrical heat source. *Frontiers in Heat and Mass Transfer*, accepted for publication, 2011.
- 7.D. Angeli, P. Levoni, and G. S. Barozzi. Numerical predictions for stable buoyant regimes within a square cavity containing a heated horizontal cylinder. *International Journal of Heat and Mass Transfer*, 51:553–565, 2008.
- 8.G. S. Barozzi, C. Bussi, and M. A. Corticelli. A fast cartesian scheme for unsteady heat diffusion on irregular domains. *Numerical Heat Transfer B*, 46:56–77, 2004.
- 9.Y. Kuznetsov. *Elements of Applied Bifurcation Theory*, volume 112 of *Applied Mathematical Sciences*. Springer-Verlag, New York, 2nd edition, 1998.

## **Decoding of Atmospheric Pressure Plasma Emission Signals for Process Control**

Victor J Law<sup>1</sup>, F T O'Neill<sup>2</sup>, D P Dowling<sup>2</sup>, J L Walsh<sup>3</sup>, F Iza<sup>3</sup>, N B Janson<sup>4</sup>, and M G Kong<sup>3</sup>

<sup>1</sup>Dublin City University, National Centre for Plasma Science and Technology, Collins Avenue, Glasnevin, Dublin 9, Dublin, Ireland.

(e-mail: [vic.law@dcu.ie](mailto:vic.law@dcu.ie))

<sup>2</sup>School of Mechanical and Materials Engineering, University College Dublin, Belfield, Dublin 4, Ireland.

<sup>3</sup>Department of Electronic and Electrical engineering, Loughborough University, Leicestershire LE11 3TU UK.

<sup>4</sup>School of Mathematics, Loughborough University, Leicestershire LE11 3TU UK.

**Abstract:** Three-dimensional phase-space representation and 3-dimensional surface imaging using single scalar time series data obtained from two very different atmospheric pressure plasma systems is presented. The process of delay embedding, Savitzky-Golay digital filtering and deconvolution of frequency-domain data is described.

**Keywords:** Plasma, Electrical measurement, Electro-acoustic, Overtones, LabVIEW.

### **1 Introduction**

Low-temperature, non-thermal atmospheric pressure plasma jets (APPJ) are being developed for surface treatment of biomedical devices, sterilisation, and therapeutic techniques, such as wound sterilisation and cancer treatment [1]. In addition to these medical applications, APPJ are now routinely employed in the automotive (car head lamps) and aerospace (fuselage and wing components) industry for surface activation of polymer prior to bonding [2]. This paper describes some of the emerging plasma electrical and electro-acoustic metrology that is being developed for the diagnostics and control of APPJ systems. In particular the requirement for extraction of information that describes the tempo-spatial heterogeneous processes. The methodology to obtain this information is currently in its infancy when compared to low pressure plasma metrology [3]. In this paper the multivariate analysis tools for the 3-dimensional phase-space representation from a single scalar time series, either of a single observable in the time-domain, or temporal-spatial deconvolutions of a single observable in the frequency-domain are given. The use of these tools to obtain measurements on two APP jet systems is presented: a hand-held plasma jet [4]; and an industrial scale computer numerical controlled PlasmaTreat OpenAir™ APPJ system [5 and 6]. By comparing the diagnostic information obtained using these two APPJ systems the robustness of the diagnostic techniques for both



laboratory and industrial scale APPJ are demonstrated.

## 2 3-D representation of a signal observation: Current

Cold APPJ pens (some times called pencils or needles) are increasingly used in many processing applications due to a distinct combination of their inherent plasma stability with excellent reaction chemistry that is often enhanced downstream. The term *cold* used here refers to temperatures of less than 50°C at the point of contact and so enables the treatment of temperature sensitive living tissue and organic polymers. An example of the helium APPJ pen examined in this study, which is driven at a drive frequency of 18 kHz, is shown in figure 3.1 and discussed in detail in references [1 and 4].

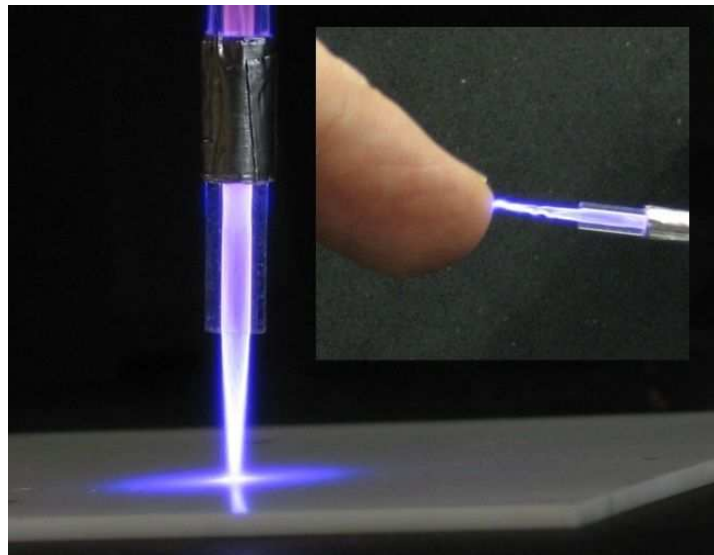


Figure 2.1: Image of a cold AAPJ pen and interaction with human figure.

This section of the paper describes one of the emerging metrology techniques that can characterise the APPJ pen's three modes of operation (chaotic, bullet and continuous). However, when there is access to only one single observable, namely, the current at the driving electrode  $I(t)$ , defining these modes becomes a challenge. Figure 2.2 details the current waveform for each of the three modes of operation. A common feature of all three modes is that their current waveform has one distinct peak every positive half cycle of the applied voltage and one current peak every negative half cycles, but later this is not always the case. The chaotic mode is observed immediately after breakdown, and an increase in the input power eventually leads to the bullet mode and then to the continuous mode. As the mode changes to bullet and then on to continuous, the current peaks become stronger and regular and finally adding an additional current peak per voltage cycle in the continuous

mode.

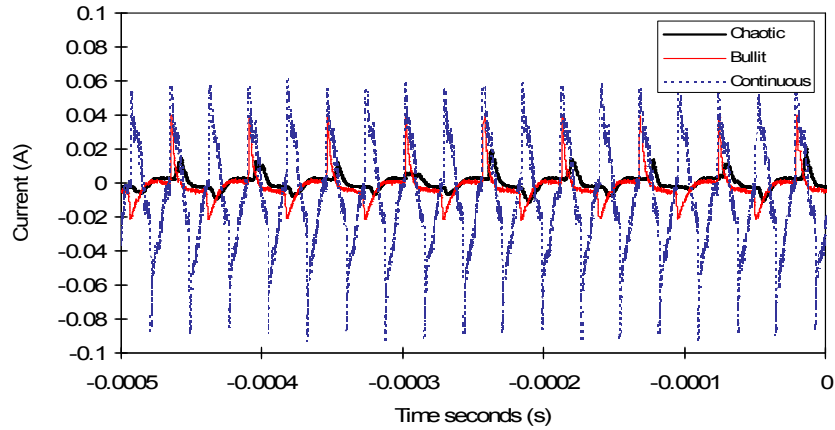


Figure 2.2: APPJ pen current waveforms in the chaotic, bullet and continuous modes.

In order to introduce a phase-space representation of the APPJ current waveform the technique of embedding is used [7]. In particular, we use the delay embedding within which the state vector at time  $t$  in the 3-dimensional phase space is reconstructed as a vector whose coordinates are the values of the single observable taken at time moments separated by a certain delay  $\tau$ , namely,  $(I(t), I(t + \tau), I(t + 2\tau), \dots, I(t + (m - 1)\tau))$ . The number  $m$  is the embedding dimension and depends on the dimension of the attractor in the original dynamical system. For visualization purposes, here we choose  $m = 3$ . The time delay  $\tau$  can be chosen by a variety of methods, but one of the most popular approaches is to calculate the mutual information from the variables  $I(t)$  and  $I(t + \tau)$  as a function of  $\tau$ , and to choose its first minimum [8]. The value of  $\tau$  obtained by this method was close to  $4\mu\text{s}$  for all datasets and was chosen for the phase-space reconstruction in this study.

Figures 2.3(*chaotic*), (*bullet*) and (*continuous*) shows 3-dimensional phase space reconstructions for the APPJ pen operating in the chaotic, bullet and continuous modes, respectively. For each mode, the phase trajectory is shown during several hundred excitation cycles. Whereas figures 2.3(*bullet*) and (*continuous*) show limit cycles (i.e. periodic attractors), figure 2.3(*chaotic*) shows a set that does not look similar to a limit cycle, nor to a low-dimensional torus representing a quasi periodic (i.e. non-chaotic) behaviour. We therefore suggest that this is a projection of a chaotic Attractor into a three-dimensional space.

An alternative to the 3-dimensional phase-space reconstruction of the current waveform is to cut the block of sequentially sampled data points in to  $n$ -frames, with each frame length equal to one complete drive frequency period,  $T$ , (where  $T = 1/f$ , followed by alignment of each frame, to a common zero-crossing-point, within the block of data. The data displayed in figure 2.2 is used for this time-domain reconstruction and has been performed in a LabVIEW program [9] where the recorded length was found to be 555 points per period of the 18 kHz

drive frequency. The computed results are shown in figure 2.4 for each of the modes (*chaotic*, *bullet* and *continuous*).

Initial comparison between the two methods visually demonstrates that both reconstructions delineate the chaotic mode. Indeed the positive current peak deterministic Jitter, as measured in the time-domain, is of the order of  $5\mu\text{s}$ , which is close to the  $\tau$  value used in the phase space reconstructions. However, the 3-dimensional phase space reconstructions provide poor visual discrimination between the bullet and continuous modes. This is because the current frequency doubling information contained in the continuous time-domain display is not clearly resolved in the phase space reconstruction. The outcome of this limited comparison suggest that a suitable attractor for representing the three APPJ pen modes can be found within the supposition of  $n$ -frames within a current waveform data block. In addition time-domain  $n$ -frame suppositions reveal the modes and therefore can be used to characterize and map the time resolved visual properties of each mode, see reference [4].

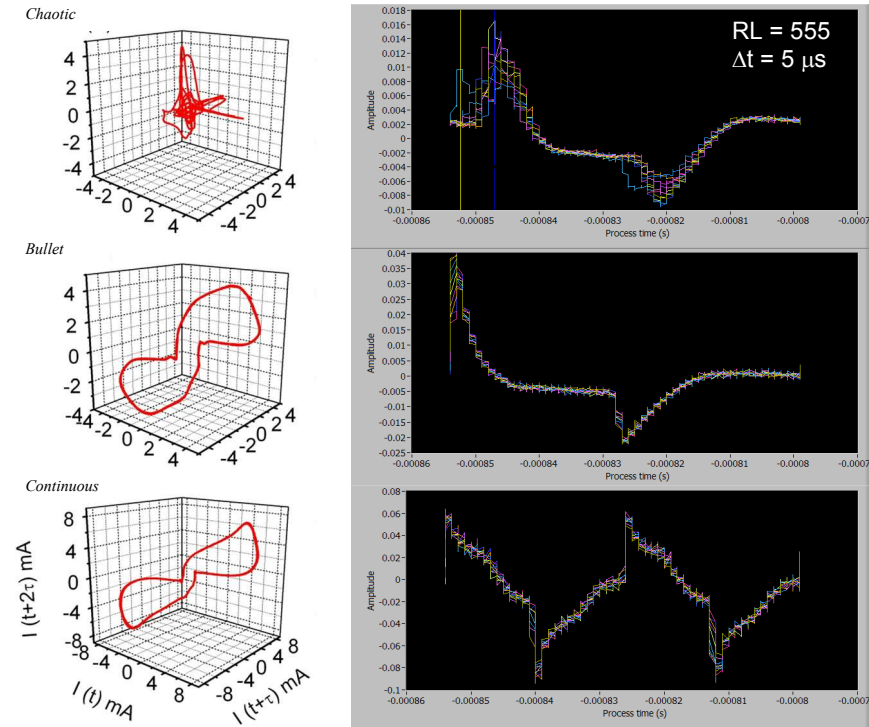


Figure 2.3: APPJ pen phase space reconstruction for each mode.

Figure 2.4: APPJ time-domain  $n$ -frame representation for each mode.

### 3 Deconvolution of a single observation: Electro-acoustic

The PlasmaTreat OpenAir™ APPJ is used worldwide and represents a typical

APPJ in the manufacturing sector. Full technical details of the APPJ are given in references [5, 6]. In this study the APPJ is electrically driven at 19 kHz and the working (ionisation) gas is Air. The first impression of this APPJ that it is much larger than the plasma pencil design, and the sound emitted by this APPJ is generally 30 dB above the environment sound level. This section is concerned with the decoding of the APPJ electro-acoustic emission [10] and the use of parts of the conditioned signal for process control.

As with reference [10] the electro-acoustic signal is captured by a microphone and sampled using a computer soundcard followed by a Fast Fourier Transform. LabVIEW 8.2 software is used to present the raw data in frequency-domain (0-60 kHz span). Within the software a Savitzky-Golay digital filter [11] is chosen to piece-by-piece smooth the raw data by least square minimisation with a polynomial function ( $m = 1$ ) within a moving window. The windowing is express in the following form, where  $k$  is the  $\pm$  sampled data points.

$$2k + 1$$

Figure 3.1a and b shows the raw un-filtered dataset (gray trace) and the filtered dataset (black trace) under plasma plume free expansion conditions. Experimentally it is found that a  $k = 10$  preserves the high Q-factor ( $f/\Delta f$  -3 dB bandwidth  $\sim 200$ ) frequency registration of the 19 kHz drive signal and its harmonics plus reduces the measurement noise floor to -100 dB that results in a signal-to-noise ratio (SRN) of 50 dB  $\pm 3$  dB: a 20 dB improvement when compared to the unfiltered dataset SRN. The second feature of note is the 3 broad peaks at 10-11, 25-30 and 45 kHz. The frequency spacing between these peaks may be represented mathematically using a quarter standing-wave closed air-column (clarinet model) [7] and so describes the longitudinal mode within the APPJ nozzle.

$$f_n = \frac{nc}{4(L + 0.6r)}$$

In the above equation,  $n$  is modulo frequency number,  $L$  is the physical length of the nozzle ( $L = 8$  mm),  $0.6r$  is the end correction, where  $r$  is the internal radius of the nozzle) and  $c_{sound}$  is the sound velocity in air. For this model the exit aperture of the nozzle defines the maximum pressure vibration, and the internal nozzle aperture, (where the compressed air is at 1.5 atmospheres) is the antinode. Using this quarter standing-wave model only the fundamental and odd number overtones are supported. For example,  $f_0$  and  $n = 3, 5$ , etc.... This model, at room temperature 25°C (where the speed of sound in air equates to 346.26 m.s<sup>-1</sup>) yields frequency values of  $f_n = 9.11$  kHz,  $f_3 = 27.33$  kHz, and  $f_5 = 45.55$  kHz. The values of  $f_n$  and  $f_3 = 3$  approximates to the broad peaks observed in figure 3.1a.

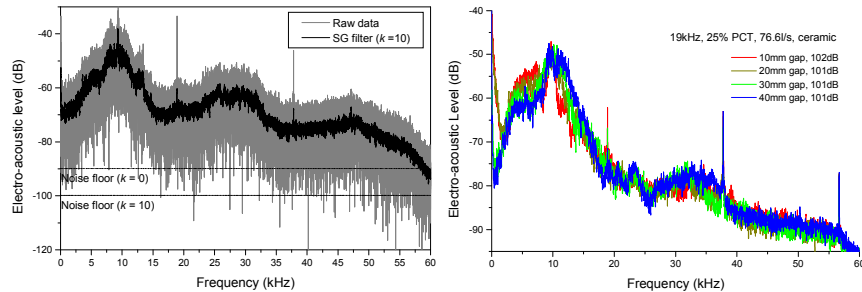


Figure 3.1a: APPJ raw signal and SG filtered signal. Figure 3.1b: APPJ SG filtered signal as a function nozzle-surface distance.

Having established the typical spectrum of the APPJ electro-acoustic emission, the focus of this section now moves to examining the electro-acoustic signal as a function APPJ nozzle to surface distance, or gap. Figure 3.1.b provides four measurements at gaps: 10, 20, 30 and 40 mm at  $k=10$ . Under these conditions the electrical drive at  $f_0 = 19$  kHz and its harmonics ( $f_2 = 38$  kHz and  $f_3 = 57$  kHz) are constant in their frequency registration. In addition the three broad peaks are still present. However a new broad peak at 4-8 kHz emerges and grows in amplitude as the gap distance is reduced. In addition, sound pressure level measurements indicate an increase of 1 dB from 101 to 102 dB.

The information obtained from this study allows the single observable electro-acoustic signal to be tested for specific conditions at discrete frequency bands. This procedure is readily implemented in LabVIEW software using lower and upper limits at the discrete frequency bands. When the signal amplitude breaches these limits, an out of bound condition fail is registered and a simple audio-visual alarm is triggered to warn the operator, or a binary code (0 or 1) from the comparator [30] may also be hard wired for data logging.

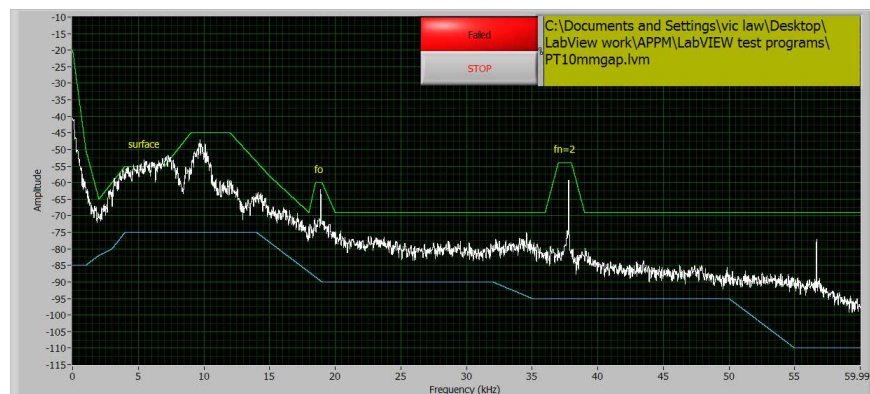


Figure 3.2: A LabVIEW screen data demonstrating how the system can be used for process control. In this case 'Fail' is associated with variation in signal in the 4 to 8 kHz frequency range.

The ability to locate a surface has many technological uses including 3-

dimensional imaging of plasma treated topographical surfaces. This section presents a LabVIEW program [10] that records the electro-acoustic emission, as the APPJ traverse back and forth across a metal work piece, and transfers the sequentially sampled data points into n-frames within a block to produce a 3-D image of the topographical surface. Figure 3.3 provides a simplified block diagram of the software where some of the control subroutines (vi(s)) have been removed for clarity.

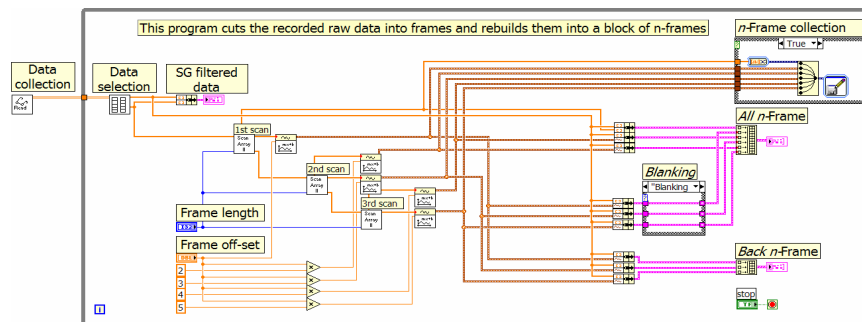


Figure 3.3: Simplified block diagram of the 3-D surface imaging software.

Figure 3.4 provides a 3-dimensional image of a 10 mm wide by 2 mm thick plate with a 2 mm diameter hole drilled in the middle of the surface. Each of the 9 scans is off-set by 2 mm, with the first scan recording the CNC positioning the APPJ to the start of the plasma process. Only the forward scans are recorded with the return blanked off. Note the acoustic discontinuity where the 2 mm hole is located.

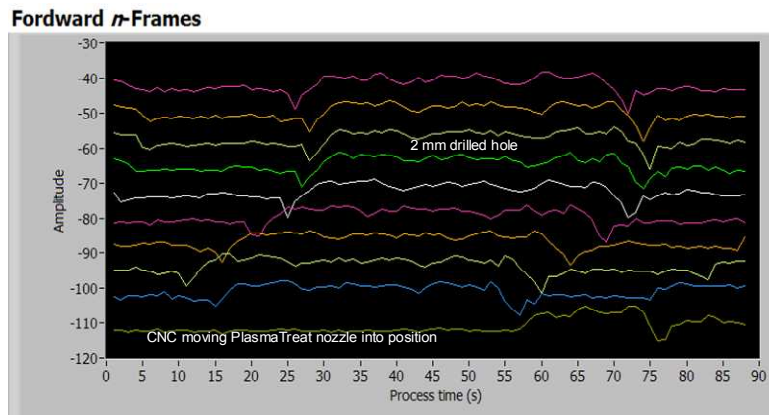


Figure 3.4: Nine scan 3-D surface image of metal surface with a 2 mm hole. Blanking turned on.

#### 4 Conclusions

Atmospheric pressure plasma jets offer enhanced quality of care at reduced cost

and will be of immense societal and commercial value. This invited paper has reviewed both time-domain current waveforms and deconvolution of electro-acoustic emission (in the frequency-domain) of two (hand-held and industrial scale APPJ systems). In the first case, 3-dimensional delay embedding was compared to periodic analysis using  $n$ -frames within a data block was compared. Both techniques provide information on the chaotic mode, with the latter yielding information on all three modes.

For the industrial scale system, single scalar time series, in the form of electro-acoustic emission is readily available. Here temporal-spatial deconvolution of the data provides information on the jet nozzle surface location and surface topology.

### Acknowledgements

This work is supported by Science foundation Ireland 08/SRC/I1411. MGK, FI and JLW thank support from EPSRC.

### References

1. M. G. Kong, G. Kroesen, G. Morfill, T. Nosenko, T. Shimizu, J. van Dijk and J. L. Zimmermann. Plasma medicine: an introductory review. *New Journal of Physics*, Vol. 9, 115012 (35pp), 2009.
2. R. Suchentrunk, H. J. Fuessler, G. Staudigl, D. Jonke, and M. Meyer. Plasma surface engineering - innovative processes and coating systems for high-quality products. *Surface and Coatings Technology*, vol. 112, no. 1-3, 351-357, 1999.
3. J. Ringwood, S. Lynn, G. Bacilli, B. Ma, E. Ragnoli and S. Mcloone. Estimation and Control in Semiconductor etch: practice and possibilities. *IEEE, Trans, Semicond, Manuf*, vol. 23, no.1, 87-96, 2010.
4. J. L. Walsh, F. Iza, N. B. Janson, V. J. Law and M. G. Kong Three distinct modes in a cold atmospheric pressure plasma jet. *J, Phys, D: Appl, Phys*, vol. 43, no. 7, 075201 (14pp), 2010.
5. D. P. Dowling, F. T. O'Neill, S. J. Langlais and V. J. Law, Influence of dc pulsed atmospheric pressure plasma jet processing conditions on polymer activation. *Plasma Process Polym*. Vol 8 no. 6, 2010. DOI: 10.1002/ppap.201000145.
6. V. J. Law, F. T. O'Neill and D. P. Dowling. Evaluation of the sensitivity of electro-acoustic measurements for process monitoring and control of an atmospheric pressure plasma jet system. *PSST*. Vol. 20, no. 3, 035024, 2011.
7. N. Packard, J. Crutchfield, D. Farmer, and R. Shaw. Geometry from time series. *Phys. Rev. Lett*, vol. 45, no. 9, 712-716, 1990.
8. A M Fraser and H L Swinney. Independent coordinates for strange attractors from mutual information. *Phys. Rev A*, vol. 33, no. 2, 1134-1140, 1986.
9. The LabVIEW software can be obtained from the principal author: [vic.law@dcu.ie](mailto:vic.law@dcu.ie)
10. V J Law, C E Nwankire, D P Dowling, and S Daniels. Acoustic emission within an atmospheric helium corona discharge jet. "Chaos Theory: Modeling, Simulation and Applications." Editors: C H. Skiadas, I Dimotikalis and C Skiadas. Publisher: World Scientific Publishing Co Pte Ltd. pp 255-264, 2011.
11. A. Savitzky, and M. J. Golay. Smoothing and differentiation of data by simplified least squared procedures. *Analytical chemistr*, vol. 36, no.8, 1627-2639, 1964.

## Sir Pinski Rides Again

Maria Ivette Gomes,<sup>1</sup> Dinis Pestana<sup>2</sup> and Pedro Pestana<sup>3</sup>

<sup>1</sup> Universidade de Lisboa and CEAUL, Lisboa, Portugal  
(E-mail: [ivette.gomes@fc.ul.pt](mailto:ivette.gomes@fc.ul.pt))

<sup>2</sup> Universidade de Lisboa and CEAUL, Lisboa, Portugal  
(E-mail: [dinis.pestana@fc.ul.pt](mailto:dinis.pestana@fc.ul.pt))

<sup>3</sup> Universidade Lusíada and CEAUL, Lisboa; Universidade Católica and CITAR,  
Porto, Portugal (E-mail: [pedro.duarte.pestana@gmail.com](mailto:pedro.duarte.pestana@gmail.com))

**Abstract.** The iterative procedure of removing “almost everything” from a triangle ultimately leading to the Sierpinski’s gasket  $\mathcal{S}$  is well-known. But what is in fact left when almost everything has been taken out? Using the Sir Pinski’s game described by Schroeder [4], we identify two dual sets of invariant points in this exquisite game, and from these we identify points left over in Sierpinski gasket. Our discussion also shows that the chaos game does not generate the Sierpinski gasket. It generates an approximation or, at most, a subset of  $\mathcal{S}$ .

**Keywords:** Sierpinski gasket, Sierpinski points, fractals, Sir Pinski game, chaos game, self-similarity, periodicity.

### 1 Introduction

Let  $\mathcal{T}$  be a triangle with vertices  $A, B, C$ , and denote  $a, b, c$  the corresponding opposite sides.

The first step of the classical iterative construction of the Sierpinski gasket is to remove the middle triangle  $\mathcal{M}_1$  with vertices  $A', B', C'$ , the middle points of  $a, b, c$ , respectively. In this first step we obtain

$$\mathcal{S}_1 = \mathcal{T} - \mathcal{M}_1 = T_1 \cup R_1 \cup L_1,$$

where  $T_1$  is the ‘top triangle’,  $R_1$  is the ‘right triangle’, and  $L_1$  is the ‘left triangle’. Observe that  $T_1, R_1$  and  $L_1$  are similar to  $\mathcal{T}$ .

In the second step we repeat the above procedure, removing  $\mathcal{M}_{2,T_1}$  in  $T_1$ , removing  $\mathcal{M}_{2,R_1}$  in  $R_1$ , and removing  $\mathcal{M}_{2,L_1}$  in  $L_1$ . With the notation  $\mathcal{M}_2 = \mathcal{M}_{2,T_1} \cup \mathcal{M}_{2,R_1} \cup \mathcal{M}_{2,L_1}$ , in this second step we obtain

$$\mathcal{S}_2 = \mathcal{S}_1 - \mathcal{M}_2 = \mathcal{T} - (\mathcal{M}_1 \cup \mathcal{M}_2).$$

$\mathcal{S}_2$  is the union of  $3^2$  triangles similar to  $\mathcal{T}$ . Each of them is easily identified using self-explanatory notations such as  $\overrightarrow{T_1 R_2}$ .

A similar procedure is indefinitely repeated: in step  $k$  we obtain  $\mathcal{S}_k$  by removing the middle triangles from each of the  $3^{k-1}$  triangles whose union is  $\mathcal{S}_{k-1}$ ; we denote  $\mathcal{M}_k$  the union of the middle triangles removed from  $\mathcal{S}_{k-1}$  to obtain  $\mathcal{S}_k$ .

Notations such as  $\overrightarrow{R_1T_2T_3L_4T_5}$  indicate in  $\mathcal{S}_5$  that we are considering the triangle obtained when in the 1st, 2nd, 3rd, 4th and 5th steps we go respectively to the right, to the top, to the top, to the left and to the top triangles of the one obtained in the previous step.

The Sierpinski gasket is

$$\mathcal{S} = \lim_{k \rightarrow \infty} \mathcal{S}_k = \bigcap_{k=1}^{\infty} \mathcal{S}_k.$$

From Banach's contractive mapping fixed point theorem it follows that the Sierpinski gasket

$$\mathcal{S} = \mathcal{T} - \bigcup_{k=1}^{\infty} \mathcal{M}_k = \psi_A(\mathcal{S}) \cup \psi_B(\mathcal{S}) \cup \psi_C(\mathcal{S}),$$

where  $\psi_A(\cdot)$  is the dilation of ratio  $1/2$  towards the top vertex  $A$ ,  $\psi_B(\cdot)$  is the dilation of ratio  $r = 1/2$  towards the left vertex  $B$ , and  $\psi_C(\cdot)$  is the dilation of ratio  $1/2$  towards the right vertex  $C$ . In other words,  $\mathcal{S}$  is the unique non-empty fixed point of the corresponding Hutchinson [2] operator  $\psi$ , where  $\psi(\mathcal{A}) = \psi_A(\mathcal{A}) \cup \psi_B(\mathcal{A}) \cup \psi_C(\mathcal{A})$ , i.e.  $\psi(\mathcal{A}) = \mathcal{A}$  if and only if  $\mathcal{A} = \mathcal{S}$ .

Thus, the use of the contracting ratio  $r = 1/2$  or of the doubling scale factor  $s = 1/r = 2$  can provide some structural information on the Sierpinski gasket.

### 1.1 The Sir Pinski Game

Let  $\mathcal{T}$  be a triangle. A player chooses a point  $P_0$  inside the triangle. Sir Pinski game consists of iteratively jumping to the points  $\{P_1, P_2, \dots\}$ , where  $P_{k+1}$  doubles the distance of  $P_k$  to its nearest vertex. The player loses at step  $n$  if  $P_0, P_1, P_2, \dots, P_{n-1} \in \mathcal{T}$  and  $P_n \notin \mathcal{T}$ .

It is obvious that  $\mathcal{M}_1$  is the set of losing points at step 1,  $\mathcal{M}_2$  is the set of losing points at step 2, and in general  $\mathcal{M}_k$  is the set of losing points at step  $k$ . Losing points are illustrated in Figure 1, that also clarifies the connection of losing points at step  $k$  with middle triangles removed at step  $k$  in the classical iterative construction of the Sierpinski gasket.

Schroeder [4] characterizes Sierpinski's gasket as the set of winning points  $\mathcal{S} = \mathcal{T} - \bigcup_{k=1}^{\infty} \mathcal{M}_k$  of Sir Pinski game.

In other words, the Sierpinski points  $S \in \mathcal{S}$  can be characterized as the set of points  $S \in \mathcal{T}$  such that  $\frac{S+A}{2}, \frac{S+B}{2}, \frac{S+C}{2} \in \mathcal{S}$ . So, starting from whatever point  $P \in \mathcal{T}$ , iteratively jumping for a point halving the distance to any of the vertices of the triangle  $\mathcal{T}$  creates an infinite sequence of points in a straight line that ultimately converges to the vertex considered. Observe however that

- if  $P \in \mathcal{S}$ , all the iterates are Sierpinski points; but, on the other hand,

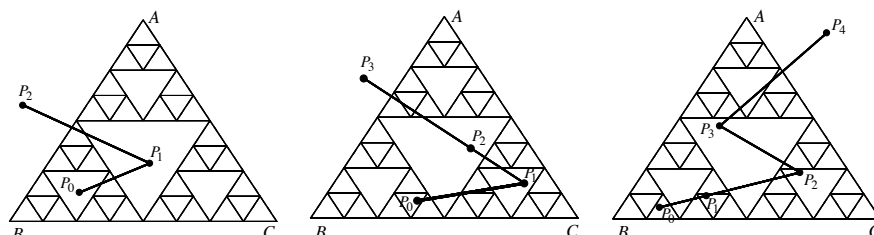


Fig. 1. Loosing points at steps 2 (left), 3 (center) and 4 (right).

- if  $P \notin \mathcal{S}$ , none of the iterates is a Sierpinski point.

In fact, the halving contractions  $\psi_i$  generate points that are nearer and nearer to Sierpinski points, but as the Sir Pinski game clearly shows, doubling the distance towards the nearest vertex ultimately leaves  $\mathcal{T}$  unless the starting point is itself a Sierpinski point.

Observe that iteratively halving (or, alternatively, doubling) the distance to a fixed vertex of the triangle  $\mathcal{T}$  creates an infinite sequence of colinear points. Hence we need some rule to use in turn, either deterministically or randomly, the different vertices in order to approximate the Sierpinski gasket  $\mathcal{S}$ . Sir Pinski game uses the deterministic rule: take the nearest vertex to the starting point/iterate, and double the distance. If the starting point is a Sierpinski point, this deterministic rule implies that we are not using a fixed vertex, and hence colinearity is broken up.

### 1.2 The Chaos Game

Barnsley [1] devised a *chaos game*, using randomness to generate subsets of the three sets  $\psi_A(\mathcal{T}), \psi_B(\mathcal{T}), \psi_C(\mathcal{T})$ : pick a starting point  $P_0$ , and generate iterates  $\{P_1, P_2, \dots\}$ , such that  $P_k$  is the midpoint of the segment whose endpoints are  $P_{k-1}$  and one of the vertices  $v_L = B, v_R = C, v_T = A$  of  $\mathcal{T}$ , randomly chosen using the discrete uniform law

$$X = \begin{cases} v_L & v_R & v_T \\ 1/3 & 1/3 & 1/3 . \end{cases}$$

This chaos game is generally presented as a device to generate the Sierpinski gasket  $\mathcal{S}$ , but in view of the above observations it produces in general an approximation of the Sierpinski gasket, since in general  $P_0 \notin \mathcal{S}$ . Observe also that even starting from a Sierpinski point, what we obtain is a subset of the Sierpinski gasket — for example, choosing  $P_0$  as the top vertex of the equilateral triangle, as in [3], page 306, will generate as iterates only vertex points of the triangles left out when middle triangles are removed, in the classical deterministic iterative construction of  $\mathcal{S}$ . This issue will be discussed later in further detail.

## 2 Invariant Sets of Points in the Sir Pinski Game and the Sierpinski Gasket

As seen in the introduction, the points  $S \in \mathcal{S}$  are easily described using the concept of self-similarity and its far-reaching consequences.

Using translation and rotation, if needed, we assume that the vertices of  $\mathcal{T}$  are  $v_L = (0, 0)$ ,  $v_R = (a, 0)$ ,  $a > 0$ , and  $v_T = (c, d)$ ,  $d > 0$ . Different characterizations of the Sierpinski set arise with different choices of  $a, c, d$ .

If  $\mathcal{T}$  is the triangle with vertices  $v_L = (0, 0)$ ,  $v_R = (1, 0)$ , and  $v_T = (0, 1)$  its Sierpinski points are, in dyadic notation,  $s = (x, 1 - x)$ , i.e. if the abscissa is  $x = 0.\nu_1\nu_2\nu_3\cdots$ , the  $k$ -th digit of the ordinate is  $1 - \nu_k$  — for instance,  $s = (0.11001011101\dots, 0.00110100010\dots)$ , cf. Peitgen *et al.* [3], p. 173.

Let  $\mathcal{T}$  be the equilateral triangle with unit height, vertices  $v_L = (0, 0)$ ,  $v_R = (2\sqrt{3}/3, 0)$ , and  $v_T = (\sqrt{3}/3, 1)$ . Schroeder [4], pp. 22–24, used a sophisticated redundant three-coordinates points affixation to show that the Sierpinski points are those with coordinates (in dyadic expansion)  $x = 0.a_1a_2a_3\cdots$ ,  $y = 0.b_1b_2b_3\cdots$ ,  $z = 0.c_1c_2c_3\cdots$ , such that  $(a_k, b_k, c_k) \in \{(1, 0, 0), (0, 1, 0), (0, 0, 1)\}$ ,  $k = 1, 2, \dots$

For our purposes it is more convenient to consider that  $\mathcal{T}$  is the equilateral triangle with unit sides, with top vertex  $A = (1/2, \sqrt{3}/2)$ , left vertex  $B = (0, 0)$ , and right vertex  $C = (1, 0)$ . Project  $A$  in the point  $A' = (1/3, 0)$ ,  $B$  in  $B' = (5/6, \sqrt{3}/6)$ , and  $C$  in  $C' = (1/3, \sqrt{3}/3)$ .

We claim that the points

- $V_1 = (3/7, 2\sqrt{3}/7)$ , intersection of  $\overline{AA'}$  with  $\overline{CC'}$ ,
- $V_2 = (5/14, \sqrt{3}/14)$ , intersection of  $\overline{AA'}$  with  $\overline{BB'}$ , and
- $V_3 = (5/7, \sqrt{3}/7)$ , intersection of  $\overline{BB'}$  with  $\overline{CC'}$ ,

are Sierpinski points, cf. Figure 2.

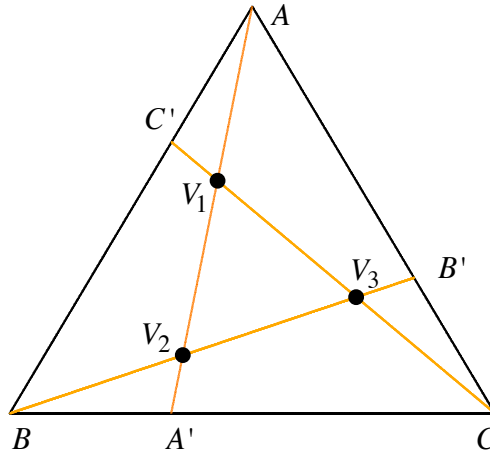
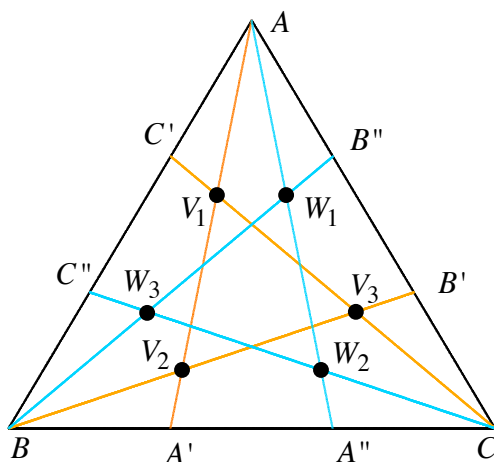


Fig. 2. Period-3 invariant Sir Pinski  $\{V_1, V_2, V_3\}$  attractor.

In fact,  $V_1$  is the midpoint of  $\overline{AV_2}$ ,  $V_2$  is the midpoint of  $\overline{BV_3}$ ,  $V_3$  is the midpoint of  $\overline{CV_1}$ , and therefore those points are winning points in the Sir Pinski game, i.e.  $\{V_1, V_2, V_3\}$  is an invariant cycle-3 attractor of Sierpinski points.

Project  $A$  in the point  $A'' = (2/3, 0)$ ,  $B$  in  $B'' = (2/3, \sqrt{3}/3)$ , and  $C$  in  $C'' = (1/6, \sqrt{3}/6)$ . Obviously, intersecting  $\overline{AA''}$  with  $\overline{BB''}$  we obtain  $W_1 = (4/7, 2\sqrt{3}/7)$ , intersecting  $\overline{AA''}$  with  $\overline{CC''}$  we obtain  $W_2 = (9/14, \sqrt{3}/14)$ , and intersecting  $\overline{BB''}$  with  $\overline{CC''}$  we obtain  $W_3 = (2/7, \sqrt{3}/7)$ . As it happens with  $\{V_1, V_2, V_3\}$ , for similar reasons,  $\{W_1, W_2, W_3\}$  is an invariant cycle-3 attractor of Sierpinski points, cf. Figure 3.



**Fig. 3.** Period-3  $\{V_1, V_2, V_3\}$  and  $\{W_1, W_2, W_3\}$  invariant Sir Pinski points attractors.  $\{A\}$ ,  $\{B\}$  and  $\{C\}$  are invariant in Sir Pinski game;  $\{A', A''\}$ ,  $\{B', B''\}$  and  $\{C', C''\}$  are period-2 invariant sets in Sir Pinski game.

*Remark 1.* If we re-scale multiplying by  $2/\sqrt{3}$  in order to have unit heights (i.e., each vertex is at distance 1 from the opposite side), the ordinates of the transformed  $V_1^*$  and  $W_1^*$  become  $4/7$ , the ordinates of the transformed  $V_2^*$  and  $W_2^*$  become  $1/7$ , and the ordinates of the transformed  $V_3^*$  and  $W_3^*$  become  $2/7$ .

Hence, if we adhere to Schroeder [4] three-coordinates system  $(x, y, z)$ , where  $x$  is the distance from the bottom side,  $y$  the distance from the left side, and  $z$  the distance from the right side, we see that the period-3 invariant points must have  $x$ -coordinate  $4/7, 1/7$  or  $2/7$ .

From the  $(2\pi/3)$ -rotational symmetry of  $\mathcal{T}$ , it follows that in Schroeder's three coordinates system

$$V_1^* = (4/7, 1/7, 2/7), V_2^* = (1/7, 2/7, 4/7), V_3^* = (2/7, 4/7, 1/7), W_1^* = (4/7, 2/7, 1/7), W_2^* = (1/7, 4/7, 2/7), \text{ and } W_3^* = (2/7, 1/7, 4/7). \quad \square$$

*Remark 2.* The points  $V_1, V_2, V_3, W_1, W_2, W_3$  lie on a circumference of radius  $\sqrt{21}/21$  centered at the barycenter  $(1/2, \sqrt{3}/6)$  of  $\mathcal{T}$ .  $\square$

*Remark 3.* Each vertex of  $\mathcal{T}$  is invariant in Sir Pinski game. Hence  $A, B, C \in \mathcal{S}$ . On the other hand, in Sir Pinski game, the image of  $A'$  is  $A''$  and vice-versa, i.e.  $\{A', A''\}$  is a period-2 invariant set, and the same holds for  $\{B', B''\}$  and  $\{C', C''\}$ .  $\mathcal{V} = \{V_1, V_2, V_3\}$  and  $\mathcal{W} = \{W_1, W_2, W_3\}$  are period-3 invariant sets (attractors) in Sir Pinski game.

Higher order periodic invariant sets do exist. For instance, using conditions  $(a-1/2)^2 + (b-\sqrt{3}/2)^2 = 4[(2a-1/2)^2 + (2b-\sqrt{3}/2)^2]$  and  $(2b - \sqrt{3}/2)/(2a - 1/2) = (\sqrt{3}/2 - b)/(a - 1/2)$  on the set of points  $\{(a, b), (2a, 2b), (1 - a, b), (1 - 2a, 2b)\}$ , so that  $(a, b) = (0.3, 0.288675)$ , we obtain the period-4 invariant set  $\{(0.3, 0.288675), (0.6, 0.636194), (0.7, 0.288675), (0.4, 0.636194)\}$ , cf. Figure 4.

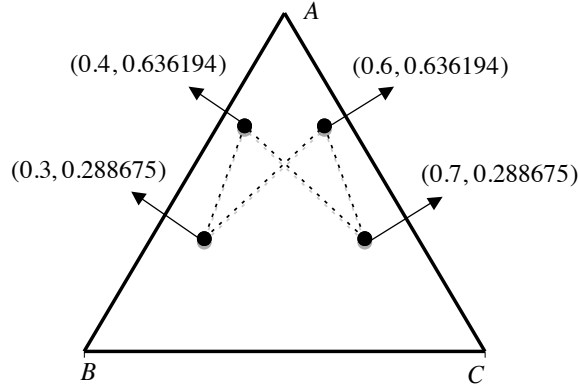


**Fig. 4.** A period-4 invariant Sir Pinski set.

Using the  $(2\pi/3)$ -rotational symmetry of  $\mathcal{T}$ , two other period-4 invariant sets are readily obtained.

More complex conditions may be used to generate other periodicity invariant sets.  $\square$

Now we perform the same construction in the  $T_1$  (Top),  $L_1$  (Left) and  $R_1$  (Right) triangles remaining once the middle triangle of  $\mathcal{T}$  is removed in step 1 of the classical construction of the Sierpinski gasket, obtaining  $2 \times 3^2$  points —  $3^2$   $V$ s and  $3^2$   $W$ s —, as shown in Figure 5. With the self-explaining addressing and notations  $V_{i,\vec{L}_1}, W_{i,\vec{L}_1}, i = 1, 2, 3$ , it is obvious that  $V_{i,\vec{L}_1} = \frac{1}{2} V_i$  and  $W_{i,\vec{L}_1} = \frac{1}{2} W_i$  — for instance,  $V_{2,\vec{L}_1} = (5/28, \sqrt{3}/28)$ ,  $V_{1,\vec{L}_1} = (4/14, 2\sqrt{3}/14)$ .

Analogously, the corresponding points in the Right triangle  $R_1$  are  $V_{i,\vec{R}_1} = (1/2, 0) + \frac{1}{2} V_i$  and  $W_{i,\vec{R}_1} = (1/2, 0) + \frac{1}{2} W_i$ , and the corresponding points in the Top triangle  $T_1$  are  $V_{i,\vec{T}_1} = (1/4, \sqrt{3}/4) + \frac{1}{2} V_i$  and  $W_{i,\vec{T}_1} = (1/4, \sqrt{3}/4) + \frac{1}{2} W_i$ . For instance,  $V_{1,\vec{T}_1} = (13/28, 11\sqrt{3}/28)$ .

The  $3^2$   $V$  points in this second stage of the construction are, following the above algorithm,  $(3/14, \sqrt{3}/7), (5/7, \sqrt{3}/7), (13/28, 11\sqrt{3}/28), (5/28, \sqrt{3}/28), (19/28, \sqrt{3}/28), (3/7, 2\sqrt{3}/7), (5/14, \sqrt{3}/14), (6/7, \sqrt{3}/14), (1/28, 9\sqrt{3}/28)$

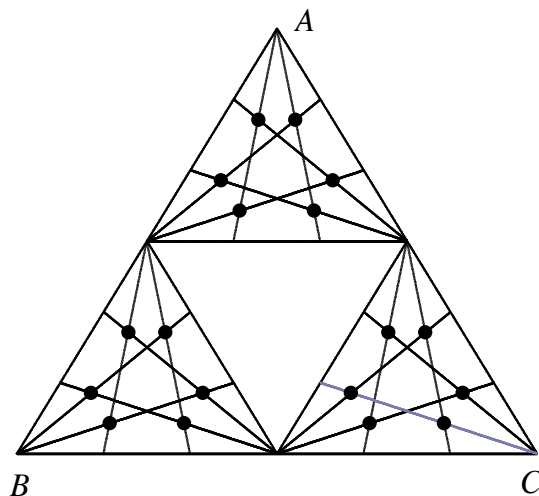


Fig. 5. More Sierpinski points, in  $T_1$ , in  $L_1$  and in  $R_1$ .

— exactly the 9 points we obtain when we compute the middle point of the segments joining each of the  $(3/7, 2\sqrt{3}/7)$ ,  $(5/14, \sqrt{3}/14)$ ,  $(5/7, \sqrt{3}/7)$   $V$  points from stage one of the construction with each of the three vertices of  $\mathcal{T}$ . Similar results hold in what concerns  $W$  points.

Continuing the procedure, in step 3 of the iterative construction of Sierpinski’s gasket we obtain  $2 \times 3^3$  points as shown in Fig. 6. (We have included some extra segments connecting points to make clear that in Sir Pinski game whatever the initial  $V$  point [respectively,  $W$  point], in a few steps we shall land in the attractor  $\mathcal{V} = \{V_1, V_2, V_3\}$  [respectively, in  $\mathcal{W} = \{W_1, W_2, W_3\}$ ].)

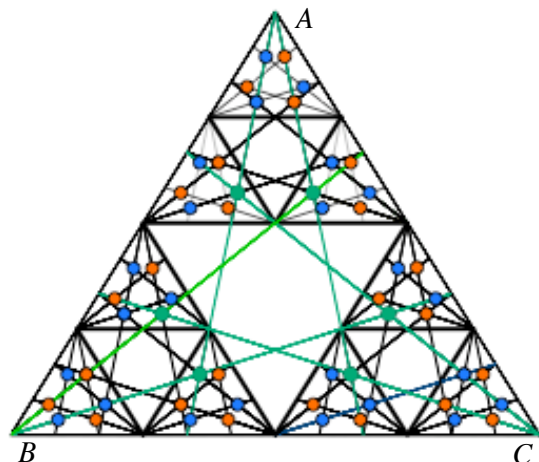


Fig. 6. More Sierpinski points, in  $T_1$ , in  $L_1$  and in  $R_1$ .

Once again the coordinates of any  $V$  or  $W$  point are easy to compute. For instance  $W_{\overrightarrow{1, L_1 T_2}} = (1/8, \sqrt{3}/8) + (1/2)^2 \times (4/7, 2\sqrt{3}/7) = (9/56, 11\sqrt{3}/56)$ , since the left vertex of the triangle whose address is  $\overrightarrow{L_1 T_2}$  is  $(1/8, \sqrt{3}/8)$ .

Using the same line of reasoning, the  $V_{i, \overrightarrow{R_1 T_2 R_3}}$  points of  $\overrightarrow{R_1 T_2 R_3}$  have coordinates  $(3/4, \sqrt{3}/8) + (1/2)^3 V_i$ , the  $W_{i, \overrightarrow{R_1 L_2 T_3 T_4}}$  points of  $\overrightarrow{R_1 L_2 T_3 T_4}$  have coordinates  $(13/16, (13/16)(\sqrt{3}/2)) + (1/2)^4 W_i$ . More generally,

- in step  $n$ , the coordinates of the original  $V$ s and  $W$ s are scaled by a factor  $(1/2)^n$ ;
- the address determines the left vertex of the triangle: a  $\overrightarrow{L_k}$  does not affect neither the abscissa nor the ordinate, a  $\overrightarrow{R_k}$  shifts the left corner  $(1/2)^k$  and does not affect the ordinate, and a  $\overrightarrow{T_k}$  adds  $(1/4)^k$  to the abscissa and  $(1/2)^k \sqrt{3}/2$  to the ordinate.

For instance, the left corner of  $\overrightarrow{T_1 L_2 L_3 R_4 R_5 T_6}$  is  $(1/4 + (1/2)^4 + (1/2)^5 + (1/4)^6, (1/2 + (1/2)^6)(\sqrt{3}/2)) = (1409/4096, 33\sqrt{3}/128)$ . Hence, the Sierpinski point  $W_{\overrightarrow{3, T_1 L_2 L_3 R_4 R_5 T_6}}$  is  $(1409/4096, 33\sqrt{3}/128) + (1/2)^6(2/7, \sqrt{3}/7) = (10119/28672, 233\sqrt{3}/896)$ .

*Remark 4.* Suppose that in the  $k$ -th step of the iterative deterministic construction of the Sierpinski gasket we focus our attention in one of the remaining triangles, for instance  $\overrightarrow{T_1 R_2 R_3 T_4 \cdots L_k}$ .

- The midpoints of the segments whose endpoints are the vertex  $A$  and the points of  $\overrightarrow{T_1 R_2 R_3 T_4 \cdots L_k}$  are the points of  $\overrightarrow{T_1 T_2 R_3 R_4 T_5 \cdots L_{k+1}}$ .
- The midpoints of the segments whose endpoints are the vertex  $B$  and the points of  $\overrightarrow{T_1 R_2 R_3 T_4 \cdots L_k}$  are the points of  $\overrightarrow{L_1 T_2 R_3 R_4 T_5 \cdots L_{k+1}}$ .
- The midpoints of the segments whose endpoints are the vertex  $C$  and the points of  $\overrightarrow{T_1 R_2 R_3 T_4 \cdots L_k}$  are the points of  $\overrightarrow{R_1 T_2 R_3 R_4 T_5 \cdots L_{k+1}}$ .

Hence, the chaos game transforms the  $V$  points [respectively, the  $W$  points] of  $\overrightarrow{T_1 R_2 R_3 T_4 \cdots L_k}$  in  $V$  points [respectively,  $W$  points] of either  $\overrightarrow{T_1 T_2 R_3 R_4 T_5 \cdots L_{k+1}}$ , or  $\overrightarrow{L_1 T_2 R_3 R_4 T_5 \cdots L_{k+1}}$  or  $\overrightarrow{R_1 T_2 R_3 R_4 T_5 \cdots L_{k+1}}$ .  $\square$

It seems useless to elaborate more on this matter to conclude that:

- In the  $k$ -th step of the classical construction of the Sierpinski gasket we may explicitly compute the coordinates of 3  $V$  points and of 3  $W$  points in each remaining triangle.
- The midpoint of any  $V$  point [respectively,  $W$  point] and any vertex of  $\mathcal{T}$  is a  $V$  point [respectively, a  $W$  point]. In other words, in the chaos game the set of  $V$  points and the set of  $W$  points do not communicate.
- In Sir Pinski game, a  $V$  starting point generates iterates that ultimately will land in  $\mathcal{V}$ , and a  $W$  starting point generates iterates that ultimately will land in  $\mathcal{W}$ . Hence all  $V$  and  $W$  points are winning points of the Sir Pinski game, i.e. they lie in  $\mathcal{S}$ . We say that  $V$  points [respectively,  $W$  points] are in the attraction domain of  $\mathcal{V}$  [respectively, of  $\mathcal{W}$ ], or that  $\mathcal{V}$  and  $\mathcal{W}$  are invariant periodicity-3 attractors in Sir Pinski game.

*Remark 5.* We also observe that subsets of 3  $V$  points and 3  $W$  points lie in circumferences centered at the barycenter of  $\mathcal{T}$ , cf. Fig. 7.  $\square$

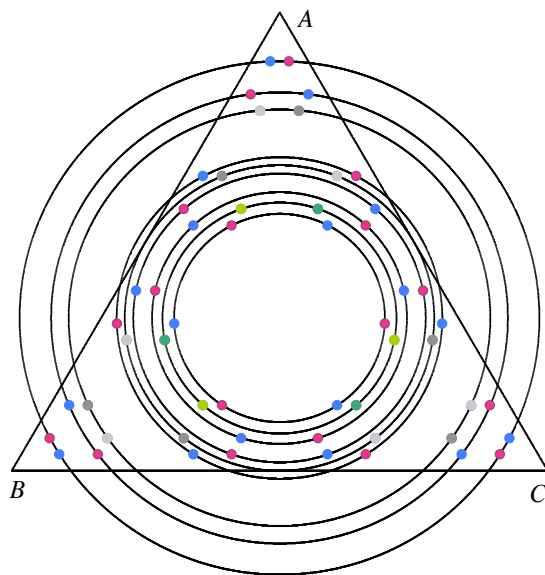


Fig. 7. A consequence of the  $\frac{2\pi}{3}$ -rotational symmetry of  $\mathcal{S}$

### 3 Concluding Remarks

#### 3.1 The Chaos Game Does Not Generate the Sierpinski Gasket

Under the heading “Randomness Creates Deterministic Shapes”, Peitgen *et al.* [3], p. 299, raise some interesting questions. The discussion in the previous section patently shows that the chaos game does not generate the Sierpinski gasket.

More precisely, if the starting point  $P_0$  is not a Sierpinski point, its descendants are not Sierpinski points, and eventually some of them computed in the initial steps are clearly spurious specks observed upon close scrutiny of the images. The set looks like the Sierpinski gasket, because the composition of contractions creates something that is very close to the Sierpinski gasket, but its intersection with the Sierpinski gasket  $\mathcal{S}$  is void.

On the other hand, our discussion shows that sets generated by the chaos game starting with a Sierpinski  $V$  point and with a Sierpinski  $W$  point are disjoint. Moreover, any of them leaves out points in the domain of attraction of invariant attractors with periodicities other than 3.

So, even with a carefully selected Sierpinski point in any of those invariant sets, the best we can get applying the chaos game is a rarefied pale image of the rich complexity of the Sierpinski gasket. The gross imperfection of the representation of points and our eyes trick us in believing we are generating the Sierpinski gasket. In fact, the representation we get is as inaccurate as the representation we get after a finite number of steps of removal of middle triangles, in the classical deterministic construction.

### 3.2 The Chaos Game and Sierpinski Polygons

The Sierpinski gasket is the sole fixed point resulting from  $\frac{1}{2}$  contractions towards the vertices  $A$ ,  $B$  and  $C$  of a triangle; for aesthetic reasons, in most situations it is worked out using an equilateral triangle.

We now consider contractions on regular polygons with  $n > 3$  vertices. Pick a point at random inside the polygon, and then draw the next point a fraction of the distance between it and a polygon vertex picked at random. Continue the process (after eventually throwing out the first few points). The result of this “chaos game” is sometimes, but not always, a fractal. In Fig. 8 we show the result of the contractions  $r_1 = \frac{1}{3}$  and  $r_1 = \frac{3}{8}$  towards the vertices of a regular pentagon.

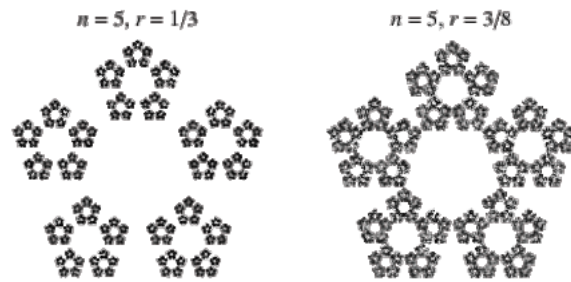


Fig. 8. Contractions  $r_1 = \frac{1}{3}$  and  $r_1 = \frac{3}{8}$  towards the vertices of a regular pentagon.

It is obvious that greater scaling factors  $s = \frac{1}{r}$  will originate “islands”, and smaller scaling factors can create overcrowded sets, with overlapping. Consequently we must refine our original definition, so that the union of contractions creates the richest fixed point without overlapping. Looking at what happens in what regards hexagons and decagons, see Fig. 9, it is easy to conclude that the ideal scaling factor for a  $n$  vertices regular polygon is

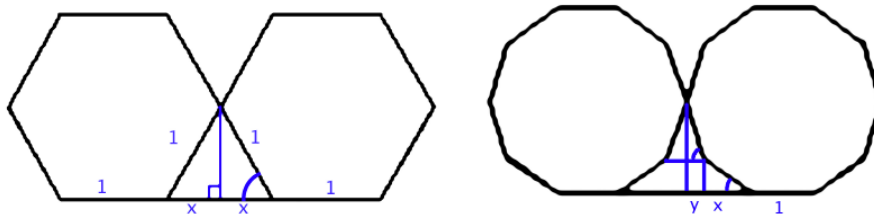


Fig. 9. Geometric rationale for computing the appropriate scaling factor.

$$s = 2 \sum_{k=0}^{\lfloor \frac{n}{4} \rfloor} \cos \frac{2\pi k}{n}.$$

(where  $\lfloor \frac{n}{4} \rfloor$  denotes the integer part of  $\frac{n}{4}$ ) — in particular, for the regular pentagon,  $s = 2(1 + \cos \frac{4\pi}{5}) \approx 2.618033989$ , and hence the ideal contraction is  $r = \frac{1}{s} \approx 0.381966011$ .

Once again the chaos game — generating the next point as the weighted mean of the current point and a vertex selected at random (i.e., using a discrete uniform law), with weights  $\frac{1}{r}$  and  $1 - \frac{1}{r}$  — gives a hint of aspect of the resulting fractal.

For instance, Fig. 10 exhibits the result of 25,000 runs of the chaos game associated with the Sierpinski octagon, generated using in R the source file

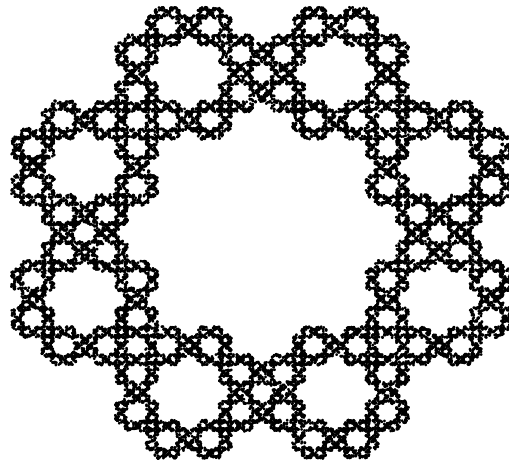


Fig. 10. Chaos game associated with Sierpinski octagon.

with the instructions

```
# Sierpinski Octagon
# 2011/01/14

#####
#####

cat("Number of runs?")
nruns<-scan(n=1)
cat("Initial point abcissa?")
x<-scan(n=1)
cat("initial point ordinate?")
y<-scan(n=1)

u<-runif(1)
if (u <= 1/8)
{
x<-0.29289322*x
```

```

y<-0.29289322*y
}
if (u>1/8 & u<=1/4)
{
x<-(0.29289322*x+0.707106781)
y<-(0.29289322*y)
}
if (u>1/4 & u<=3/8)
{
x<-(0.29289322*x+0.707106781*1.70710678 )
y<-(0.29289322*y+0.707106781*0.70710678)
}
if (u>3/8 & u<=1/2)
{
x<-(0.29289322*x+0.707106781*1.70710678 )
y<-(0.29289322*y+0.707106781*1.70710678)
}
if (u>1/2 & u<=5/8)
{
x<-(0.29289322*x+ 0.707106781 )
y<-(0.29289322*y+0.707106781*2.41421356)
}
if (u>5/8 & u<=3/4)
{
x<-(0.29289322*x )
y<-(0.29289322*y+0.707106781*2.41421356)
}
if (u>3/4 & u<=7/8)
{
x<-(0.29289322*x-0.707106781*0.70710678 )
y<-(0.29289322*y+0.707106781*1.70710678)
}
if (u>7/8)
{
x<-(0.29289322*x-0.707106781*0.70710678 )
y<-(0.29289322*y+0.707106781*0.70710678)
}

plot(x,y,xlim=c(-1,2),ylim=c(0,3),pch=20, cex=0.2,
xaxt="n",yaxt="n",xlab="",ylab="",bty="n")

for(i in 1:nruns)
{
u<-runif(1)

if (u <= 1/8)
{

```

```

x<-0.29289322*x
y<-0.29289322*y
}
if (u>1/8 & u<=1/4)
{
x<-(0.29289322*x+0.707106781)
y<-(0.29289322*y)
}
if (u>1/4 & u<=3/8)
{
x<-(0.29289322*x+0.707106781*1.70710678 )
y<-(0.29289322*y+0.707106781*0.70710678)
}
if (u>3/8 & u<=1/2)
{
x<-(0.29289322*x+0.707106781*1.70710678 )
y<-(0.29289322*y+0.707106781*1.70710678)
}
if (u>1/2 & u<=5/8)
{
x<-(0.29289322*x+ 0.707106781 )
y<-(0.29289322*y+0.707106781*2.41421356)
}
if (u>5/8 & u<=3/4)
{
x<-(0.29289322*x )
y<-(0.29289322*y+0.707106781*2.41421356)
}
if (u>3/4 & u<=7/8)
{
x<-(0.29289322*x-0.707106781*0.70710678 )
y<-(0.29289322*y+0.707106781*1.70710678)
}
if (u>7/8)
{
x<-(0.29289322*x-0.707106781*0.70710678 )
y<-(0.29289322*y+0.707106781*0.70710678)
}

points(x,y,pch=20,cex=0.25)
for (j in 1:25000) a=1
}

```

4e (we used the approximation  $r = 2 + \sqrt{2} \approx 3.414213562$  for the scaling factor, and the weights 0.292893219 for the current point and 0.707106781 for the randomly chosen vertex in order to compute weighted means at each step). This code is easily modified for any  $n$ , using the appropriate scaling factor.

Once again, for any  $n$  this generates a subset or an approximation of the fixed point of an Hutchinson operator which is the union of contractions towards each of the vertices of the polygon, with appropriate scaling factor, but is not, in fact, the (extended) Sierpinski fixed point.

## References

1. M. F. Barnsley. *Fractals Everywhere*, Academic Press, New York, 1988.
2. J. Hutchinson, Fractals and self-similarity, *Indiana University Journal of Mathematics*, vol. 30, pp. 713-747, 1981.
3. H.-O. Peitgen, H. Jürgens, and D. Saupe. *Chaos and Fractals: New Frontiers of Science*, 2nd ed., Springer Verlag, New York, 2004.
4. M. Schroeder. *Fractals, Chaos, Power Laws: Minutes from an Infinite Paradise*, Dover, New York, 2009.

**FCT** *This research has been supported by National Funds through FCT — Fundação para a Ciência e a Tecnologia, project PEst-OE/MAT/UI0006/2011, and PTDC/FEDER.*

# Some considerations on the usefulness to approximate a Markov chain by a solution of a stochastic differential equation

Gabriel V. Orman and Irinel Radomir

”Transilvania” University of Braşov, 500091 Braşov, Romania  
(E-mail: ogabriel@unitbv.ro)

**Abstract.** In this paper some problems regarding to the Markov property are discussed. Among other things, it is presented the extended Markov property, as it has been synthesized by Kiyosi Itô. Also, it will be emphasized the possibility to approximate a Markov chain by a solution of a stochastic differential equation in a problem of financial risk.

**Keywords:** Brownian motion, stochastic differential equations, Markov process, transition probabilities .

## 1 Introduction

As it can be observed, in the last time, a great interest has been shown to some topics relating to stochastic approximation procedures and their applications.

Generally speaking, it can be considered a problem where computation is split among several processors, operating and transmitting data to one another asynchronously. Such algorithms are only being to come into prominence, due to both the developments of decentralized processing and applications where each of several locations might control or adjusted *local variable* but the criterion of concern is global. For example a current *decentralized* application is in *Q*-learning where the component update at any time depends on the state of a Markov process.

After Robbins & Monro laid the foundations of the stochastic approximations procedures, several problems have been developed especially by Z. Schuss, H.J. Kushner, K. Itô, H.P. McKean Jr., M.T. Wasan, B. Øksendal, N. Ikeda, S. Watanabe. Results on almost sure convergence of stochastic approximation processes are often proved by a separation of deterministic (pathwise) and stochastic considerations. The basic idea is to show that a ”distance” between estimate and solution itself has the tendency to become smaller.

In the last decades a great interest has been shown to the investigations of applications in many diverse areas, and this has accelerated in the last time, with new applications. Shortly speaking, the basic stochastic approximation



algorithm is nothing but a stochastic difference equation with a small step size, and the basic questions for analysis concern its qualitative behaviour over a long time interval, such as convergence and rate of convergence.

When a stochastic differential equation is considered if it is allowed for some randomness in some of its coefficients, it will be often obtained a so-called *stochastic differential equation* which is a more realistic mathematical model of the considered situation. Many practical problems conduct us to the following notion: *the equation obtained by allowing randomness in the coefficients of a differential equation is called a "stochastic differential equation"*. Thus, it is clear that any solution of a stochastic differential equation must involve some randomness. In other words one can hope to be able to say something about the probability distribution of the solutions.

On the other hand, as it is known, a precise definition of the Brownian motion involves a measure on the path space, such that it is possible to put the Brownian motion on a firm mathematical foundation. Numerous scientific works has been done on its applications in diverse areas including among other things stability of structures, solid-state theory, population genetics, communications, and many other branches of the natural sciences, social sciences and engineering. We emphasize here many contributions due to P. Lévy, K. Itô, H.P. McKean, Jr., S. Kakutani, H.J. Kushner, A.T. Bharucha-Reid and other.

If we refer, for example, to some aspects in genetics, as the approximation of Markov chains by solutions of some stochastic differential equations to determine the probability of extinction of a genotype, then the Markovian nature of the problem will be pointed out, and we think that this is a very important aspect.

In this paper we shall discuss firstly some aspects relating to the approximation in the study of Markov processes and Brownian motion. Such problems were developed particularly by Z. Schuss, H.J. Kushner, K. Itô, H.P. McKean Jr., B. Øksendal, M.T. Wasan.

Then we refer to some aspects regarding to the Markov property in a vision of K. Itô. And finally, as an application, a problem of stochastic approximation in the risk analysis, based on a study of Hu Yaozhong, in connection with a stochastic differential equation, is considered.

## 2 In short about stochastic differential equations

We know that to describe the motion of a particle driven by a *white noise* type of force (due to the collision with the smaller molecules of the fluid) the following equation is used

$$\frac{d\mathbf{v}(t)}{dt} = -\beta\mathbf{v}(t) + \mathbf{f}(t) \quad (1)$$

where  $\mathbf{f}(t)$  is the white noise term.

The equation (1) is referred to as the *Langevin's equation*. Its solution is the following

$$y(t) = y_0 e^{-\beta t} + e^{-\beta t} \int_0^t e^{-\beta s} \mathbf{f}(s) ds. \quad (2)$$

If we denote by  $\mathbf{w}(t)$  the Brownian motion (see the next section), then it is given by

$$\mathbf{w}(t) = \frac{1}{q} \int_0^t \mathbf{f}(s) ds, \tag{3}$$

so that  $\mathbf{f}(s) = \frac{q d\mathbf{w}(s)}{ds}$ . But  $\mathbf{w}(t)$  is nowhere differentiable, such that  $\mathbf{f}(s)$  is not a function. Therefore, the solution (2), of Langevin’s equation, is not a well-defined function. This difficulty can be overcome, in the simple case, as follows. Integrating (2) by parts, and using (3), it results

$$y(t) = y_0 e^{-\beta t} + q\mathbf{w}(t) - \beta q \int_0^t e^{-\beta(t-s)} \mathbf{w}(s) ds. \tag{4}$$

But all functions in (4) are well defined and continuous, such that the solution (3) can be interpreted by giving it the meaning of (4). Now, such a procedure can be generalized in the following way. Let us given two functions  $f(t)$  and  $g(t)$  that are considered to be defined for  $a \leq t \leq b$ . For any partition  $P : a \leq t_0 < t_1 < \dots < t_n$ , we denote

$$S_P = \sum_{i=1}^n f(\xi_i)[g(t_i) - g(t_{i-1})],$$

where  $t_{i-1} \leq \xi_i \leq t_i$ . If a limit exists

$$\lim_{|P| \rightarrow 0} S_P = I$$

where  $|P| = \max_{1 \leq i \leq n} (t_i - t_{i-1})$ , then it is said that  $I$  is the *Stieltjes integral* of  $f(t)$  with respect to  $g(t)$ . It is denoted

$$I = \int_a^b f(t) dg(t).$$

Now the stochastic differential equation

$$\begin{aligned} dx(t) &= a(x(t), t)dt + b(x(t), t)dw(t) \\ x(0) &= x_0 \end{aligned} \tag{5}$$

is defined by the Itô integral equation

$$x(t) = x_0 + \int_0^t a(x(s), s)ds + \int_0^t b(x(s), s)dw(s). \tag{6}$$

The simplest example of a stochastic differential equation is the following equation

$$\begin{aligned} dx(t) &= a(t)dt + b(t)dw(t) \\ x(0) &= x_0 \end{aligned} \tag{7}$$

which has the solution

$$x(t) = x_0 + \int_0^t a(s)ds + \int_0^t b(s)dw(s).$$

The *transition probability density* of  $x(t)$  is a function  $p(x, s; y, t)$  satisfying the condition

$$P(x(t) \in A | x(s) = x) = \int_A p(x, s; y, t)dy$$

for  $t > s$  where  $A$  is any set in  $R$ . It is supposed that  $a(t)$  and  $b(t)$  are deterministic functions.

The stochastic integral

$$\chi(t) = \int_0^t b(s)dw(s)$$

is a limit of linear combinations of independent normal variables

$$\sum_i b(t_i)[w(t_{i+1}) - w(t_i)].$$

Thus, the integral is also a normal variable.

But, then

$$\chi(t) = x(t) - x_0 - \int_0^t a(s)ds$$

is a normal variable, and therefore

$$p(x, s; y, t) = \frac{1}{\sqrt{2\pi\sigma}} e^{-\frac{(y-m)^2}{2\sigma}}$$

where

$$m = E(x(t) | x(s) = x).$$

Now

$$E(x(t) | x(s) = x) = x + \int_s^t a(u)du$$

is the expectation of the stochastic integral vanishes.

And the variance is given by the relation

$$\sigma = Var x(t) = E \left[ \int_s^t b(u)dw(u) \right]^2 = \int_s^t b^2(u)du.$$

In conclusion,  $p(x, s; y, t)$  is given by the following equation

$$p(x, s; y, t) = \left[ 2\pi \int_s^t b^2(u)du \right]^{-\frac{1}{2}} \cdot e^{-\frac{\left( y - x - \int_s^t a(u)du \right)^2}{2 \int_s^t b^2(u)du}}.$$

[For more details and proofs see, for example: G. Da Prato and J. Zabczyk[3], G. Da Prato[4], N. Ikeda and S. Watanabe[6], K. Itô and H. P. McKean Jr.[8], B. Øksendal[13], Z. Schuss[26]].

### 3 Brownian motion

Brownian motion, used especially in Physics, is of ever increasing importance not only in Probability theory but also in classical Analysis. Its fascinating properties and its far-reaching extension of the simplest normal limit theorems to functional limit distributions acted, and continue to act, as a catalyst in random Analysis. It is probable the most important stochastic process. As some authors remarks too, the Brownian motion reflects a perfection that seems closer to a law of nature than to a human invention.

In 1828 the English botanist Robert Brown observed that pollen grains suspended in water perform a continual swarming motion. The chaotic motion of such a particle is called *Brownian motion* and a particle performing such a motion is called a *Brownian particle*.

The first important applications of Brownian motion were made by L. Bachelier and A. Einstein. L. Bachelier derived (1900) the law governing the position of a single grain performing a 1-dimensional Brownian motion starting at  $a \in R^1$  at time  $t = 0$

$$P_a[x(t) \in db] = g(t, a, b)db \tag{8}$$

where  $(t, a, b) \in (0, +\infty) \times R^2$  and  $g$  is the Green (or the *source*) function

$$g(t, a, b) = \frac{1}{t\sqrt{2\pi}} e^{-\frac{(b-a)^2}{2t^2}}$$

of the problem of heat flow

$$\frac{\partial u}{\partial t} = \frac{1}{2} \frac{\partial^2 u}{\partial a^2}, \quad (t > 0).$$

Bachelier also pointed out the Markovian nature of the Brownian path but he was unable to obtain a clear picture of the Brownian motion and his ideas were unappreciated at that time. This because a precise definition of the Brownian motion involves a measure on the path space, and it was not until 1908-1909 when the works of É. Borel and H. Lebesgue have been appeared. Beginning with this moment was possible to put the Brownian motion on a firm mathematical foundation and this was achieved by N. Wiener in 1923.

It is very interesting that A. Einstein also derived (8) in 1905 from statistical mechanical considerations and applied it to the determination of molecular diameters. He wanted also to model the movement of a particle suspended in a liquid. Einstein's aim was to provide a means of measuring Avogadro's number, the number of molecules in a mole of gas, and experiments suggested by Einstein proved to be consistent with his predictions.

We remind, for example, the following aspect. Let us consider that  $\mathbf{x}(t)$  is the notation for the displacement of the Brownian particle. Then, the probability density of this displacement, for sufficiently large values of  $t$ , is as follows

$$p(\mathbf{x}, t, \mathbf{x}_0, \mathbf{v}_0) \approx \frac{1}{(4\pi Dt)^{\frac{3}{2}}} e^{-\frac{|\mathbf{x}-\mathbf{x}_0|^2}{4Dt}} \tag{9}$$

where  $D$  is

$$D = \frac{kT}{m\beta} = \frac{kT}{6\pi a\eta} \quad (10)$$

and is referred to as the *diffusion coefficient*.

Furthermore it results that  $p(\mathbf{x}, t, \mathbf{x}_0, \mathbf{v}_0)$  satisfies the diffusion equation given below

$$\frac{\partial p(\mathbf{x}, t, \mathbf{x}_0, \mathbf{v}_0)}{\partial t} = D\Delta p(\mathbf{x}, t, \mathbf{x}_0, \mathbf{v}_0). \quad (11)$$

The expression of  $D$  in (10) was obtained by A. Einstein.

*Remark 1.* From physics it is known the following result due to Maxwell: Let us suppose that the energy is proportional to the number of particles in a gas and let us denoted  $E = \gamma n$ , where  $\gamma$  is a constant independent of  $n$ . Then,

$$\begin{aligned} P\{a < v_i^1 < b\} &= \frac{\int_a^b \left(1 - \frac{x^2 m}{2\gamma n}\right)^{\frac{3n-3}{2}} dx}{\int_{-\left(\frac{2\gamma n}{m}\right)^{\frac{1}{2}}}^{+\left(\frac{2\gamma n}{m}\right)^{\frac{1}{2}}} \left(\frac{1 - x^2 m}{2\gamma n}\right)^{\frac{3n-3}{2}} dx} \rightarrow \\ &\rightarrow \left(\frac{3m}{4\pi\gamma}\right)^{\frac{1}{2}} \int_a^b e^{-\frac{3mx^2}{4\gamma}} dx. \end{aligned}$$

Now, for  $\gamma = \frac{3kT}{2}$  the following Maxwell's result is found

$$\lim_{n \rightarrow \infty} P\{a < v_i^1 < b\} = \left(\frac{m}{2\pi kT}\right)^{\frac{1}{2}} \int_a^b e^{-\frac{mx^2}{2kT}} dx.$$

$T$  is called the "absolute temperature", while  $k$  is the "Boltzmann's constant".

[For details and proofs see K. Itô and H. P. McKean Jr.[8], Z. Schuss[26], D. W. Stroock[27], G. V. Orman[20]].

## 4 On Markov property

In some previous papers we have dicussed on Markov processes in a vision of Kiyosi Itô. In this section we shall continue this discussion by considering the extended Markov property.

More details and other aspects can be found in K. Itô[7],[9], K. Itô and H. P. McKean Jr.[8], D. W. Stroock[27], A. T. Bharucha-Reid[2].

Let  $S$  be a *state space* and consider a particle which moves in  $S$ . Also, suppose that the particle starting at  $x$  at the present moment will move into the set  $A \subset S$  with probability  $p_t(x, A)$  after  $t$  units of time, "irrespectively of

its past motion”, that is to say, this motion is considered to have a *Markovian character*.

The *transition probabilities* of this motion are  $\{p_t(x, A)\}_{t,x,A}$  and is considered that the time parameter  $t \in T = [0, +\infty)$ .

The state space  $S$  is assumed to be a *compact Hausdorff space with a countable open base*, so that it is homeomorphic with a compact separable metric space by the Urysohn’s metrization theorem. The  $\sigma$ -field generated by the open space (the topological  $\sigma$ -field on  $S$ ) is denoted by  $K(S)$ . Therefore, a *Borel set* is a set in  $K(S)$ .

The *mean value*

$$m = M(\mu) = \int_R x \mu(dx)$$

is used for the center and the scattering degree of an one-dimensional probability measure  $\mu$  having the second order moment finite, and the *variance* of  $\mu$  is defined by

$$\sigma^2 = \sigma^2(\mu) = \int_R (x - m)^2 \mu(dx).$$

On the other hand, from the Tchebychev’s inequality, for any  $t > 0$ , we have

$$\mu(m - t\sigma, m + t\sigma) \leq \frac{1}{t^2},$$

so that several properties of 1-dimensional probability measures can be derived.

Note that in the case when the considered probability measure has no finite second order moment,  $\sigma$  becomes useless. In such a case one can introduce the central value and the dispersion that will play similar roles as  $m$  and  $\sigma$  for general 1-dimensional probability measures.

*Remark 2.* We recall that J. L. Doob defined the *central value*  $\gamma = \gamma(\mu)$  as being the real number  $\gamma$  which verifies the following relation

$$\int_R \arctg(x - \gamma) \mu(dx) = 0.$$

Here, the existence and the uniqueness of  $\gamma$  follows from the fact that  $\arctg(x - \gamma)$  is continuous and decreases strictly from  $\frac{\pi}{2}$  to  $-\frac{\pi}{2}$ , for  $x$  fixed, as  $\gamma$  moves from  $-\infty$  to  $+\infty$ .

The *dispersion*  $\delta$  is defined as follows

$$\delta = \delta(\mu) = -\log \int \int_{R^2} e^{-|x-y|} \mu(dx) \mu(dy).$$

We will assume that the transition probabilities  $\{p_t(x, A)\}_{t \in T, x \in S, A \in K(S)}$  satisfy the following conditions:

- (1) for  $t$  and  $A$  fixed,
  - a) the transition probabilities are Borel measurable in  $x$ ;
  - b)  $p_t(x, A)$  is a probability measure in  $A$ ;
- (2)  $p_0(x, A) = \delta_x(A)$  (i.e. the  $\delta$ -measure concentrated at  $x$ );

(3)  $p_t(x, \cdot) \xrightarrow{weak} p_t(x_0, \cdot)$  as  $x \rightarrow x_0$  for any  $t$  fixed, that is

$$\lim_{x \rightarrow x_0} \int f(y)p_t(x, dy) = \int f(y)p_t(x_0, dy)$$

for all continuous functions  $f$  on  $S$ ;

- (4)  $p_t(x, U(x)) \rightarrow 1$  as  $t \searrow 0$ , for any neighborhood  $U(x)$  of  $x$ ;  
 (5) the Chapman-Kolmogorov equation holds:

$$p_{s+t}(x, A) = \int_S p_t(x, dy)p_s(y, A).$$

The *transition operators* can be defined in a similar manner. Consider  $C = C(S)$  to be the space of all continuous functions (it is a separable Banach space with the supremum norm).

The operators  $p_t$ , defined by

$$(p_t f)(x) = \int_S p_t(x, dy)f(y), \quad f \in C$$

are called *transition operators*.

The conditions for the transition probabilities can be adapted to the transition operators, but we do not insist here.

*Remark 3.* Let us observe that the conditions (1) – (5) above are satisfied for "Brownian transition probabilities". One can define

$$p_t(x, dy) = \frac{1}{t\sqrt{2\pi}} e^{-\frac{(y-x)^2}{2t^2}} dy \quad \text{in } R$$

$$p_t(\infty, A) = \delta_\infty A.$$

Now the Markov process can be defined.

**Definition 1** *A Markov process is a system of stochastic processes*

$$\{X_t(\omega), t \in T, \omega \in (\Omega, K, P_a)\}_{a \in S},$$

that is for each  $a \in S$ ,  $\{X_t\}_{t \in S}$  is a stochastic process defined on the probability space  $(\Omega, K, P_a)$ .

The transition probabilities of a Markov process will be denoted by  $\{p(t, a, B)\}$ . Now let us denote by  $\{H_t\}$  the transition semigroup and let  $R_\alpha$  be the resolvent operator of  $\{H_t\}$ .

The next results shows that  $p(t, a, B)$ ,  $H_t$  and  $R_\alpha$  can be expressed in terms of the process as follows:

**Theorem 1** *Let  $f$  be a function in  $C(S)$ . Then*

- i)  $p(t, a, B) = P_a(X_t \in B)$ .
- ii) For  $E_a(\cdot) = \int_\Omega \cdot P_a(d\omega)$  one has  $H_t f(a) = E_a(f(X_t))$ .
- iii)  $R_\alpha f(a) = E_a\left(\int_0^\infty e^{-\alpha t} f(X_t) dt\right)$ .

*Proof.* One can observe that *i*) and *ii*) follow immediately.

To prove *iii*), we will use the following equality:

$$R_\alpha f(a) = \int_0^\infty e^{-\alpha t} H_t f(a) dt = \int_0^\infty e^{-\alpha t} E_a(f(H_t)) dt.$$

Since  $f(X_t(\omega))$  is right continuous in  $t$  for  $\omega$  fixed, and measurable in  $\omega$  for  $t$  fixed, it is therefore measurable in the pair  $(t, \omega)$ . Thus, we can use Fubini's theorem and therefore we obtain

$$R_\alpha f(a) = E_a \left( \int_0^\infty e^{-\alpha t} f(X_t) dt \right),$$

which proves *iii*).

**Definition 2** The operator  $\theta_t : \Omega \rightarrow \Omega$  defined by

$$(\theta_t \omega)(s) = \omega(s + t)$$

for every  $s \in T$  is called the “shift operator”.

Obviously, the operator  $\theta_t$  satisfies the property

$$\theta_{t+s} = \theta_t \theta_s,$$

called the *semigroup property*.

For  $\mathcal{C}$  a  $\sigma$ -field on  $\Omega$ , the space of all bounded  $\mathcal{C}$ -measurable functions will be denoted by  $\mathbf{B}(\Omega, \mathcal{C})$ , or simple  $\mathbf{B}(\mathcal{C})$ .

#### 4.1 The classical and the extended Markov property

Now the *Markov property* is expressed in the theorem below.

**Theorem 2** Let be given  $\Gamma \in K$ . The following is true

$$P_a(\theta_t \omega \in \Gamma | K_t) = P_{X_t(\omega)}(\Gamma) \quad a.s.(P_a);$$

that is to say

$$P_a(\theta_t^{-1} \Gamma | K_t) = P_{X_t(\omega)}(\Gamma).$$

*Remark 4.* The following notation can be used

$$P_{X_t(\omega)}(\Gamma) = P_b(\Gamma)|_{b=X_t(\omega)}.$$

Now, to prove the theorem, it will be suffice to show that

$$P_a(\theta_t^{-1} \Gamma \cap D) = E_a(P_{X_t}(\Gamma), D) \tag{12}$$

for  $\Gamma \in K$  and  $D \in K_t$ .

Three cases can be distinguished.

1). Let us consider  $\Gamma$  and  $D$  as follows:

$$\Gamma = \{X_{s_1} \in B_1\} \cap \{X_{s_2} \in B_2\} \cap \dots \cap \{X_{s_n} \in B_n\},$$

and

$$D = \{X_{t_1} \in A_1\} \cap \{X_{t_2} \in A_2\} \cap \cdots \cap \{X_{t_m} \in A_m\}$$

with

$$\begin{aligned} 0 &\leq s_1 < s_2 < \cdots < s_n \\ 0 &\leq t_1 < t_2 < \cdots < t_m \leq t \end{aligned}$$

and  $B_i, A_j \in K(S)$ .

Now it will be observed that the both sides in (12) are expressed as integrals on  $S^{m+n}$  in terms of transition probabilities. Thus, one can see that they are equal.

**2).** Let now be  $\Gamma$  as in the case **1)** and let us denote by  $D$  a general member of  $K_t$ . For  $\Gamma$  fixed the family  $\mathcal{D}$  of all  $D$ 's satisfying (12) is a Dynkin class. If  $\mathcal{M}$  is the family of all  $M$ 's in the case **1)** then, this family is multiplicative and  $\mathcal{M} \subset \mathcal{D}$ . In this way it follows

$$\mathcal{D}(\mathcal{M}) \subset \mathcal{D} = K(\mathcal{M}) = K_t$$

and one can conclude that, for  $\Gamma$  in the case **1)** and for  $D$  general in  $K_t$ , the equality (12) holds.

**3).** (*General case.*) This case can be obtained in a same manner from **2)** by fixing an arbitrary  $D \in K_t$ .

It will be obtained that  $P_a(\Gamma)$  is Borel measurable in  $a$  for any  $\Gamma \in K$ .

### Corollaire 1

$$\begin{aligned} E_a(G \circ \theta_t, D) &= E_a(E_{X_t}(G), D) \quad \text{for } G \in \mathbf{B}(K), D \in K_t, \\ E_a(F \cdot (G \circ \theta_t)) &= E_a(F \cdot E_{X_t}(G)) \quad \text{for } G \in \mathbf{B}(K), F \in \mathbf{B}(K_t), \\ E_a(G \circ \theta_t | K_t) &= E_{X_t}(G) \quad (a.s.)(P_a) \quad \text{for } G \in \mathbf{B}(K). \end{aligned}$$

But it is interesting to see that the Markov property can be extended, as it is given in the following theorem, according to K. Itô:

**Theorem 3** (*The extended Markov property*).

$$P_a(\theta_t \omega \in \Gamma | K_{t+}) = P_{X_t}(\Gamma) \quad a.s. (P_a)$$

for  $\Gamma \in K$ .

*Proof.* Let us come back to the equality (12) before. Now it will be proved for  $D \in K_{t+}$ . To this end the following equality will be shown:

$$\begin{aligned} E_a(f_1(X_{s_1}(\theta_t \omega)) \cdots f_n(X_{s_n}(\theta_t \omega)), D) &= \\ &= E_a(E_{X_t}(f_1(X_{s_1}) \cdots f_n(X_{s_n})), D) \end{aligned} \quad (13)$$

for  $f_i \in C(S)$ ,  $D \in K_{t+}$  and  $0 \leq s_1 < s_2 < \cdots < s_n$ .

But  $D \in K_{t+h}$  for  $h > 0$ , so that by Corollary 1 it results

$$\begin{aligned} E_a(f_1(X_{s_1}(\theta_{t+h} \omega)) \cdots f_n(X_{s_n}(\theta_{t+h} \omega)), D) &= \\ &= E_a(E_{X_{t+h}}(f_1(X_{s_1}) \cdots f_n(X_{s_n})), D). \end{aligned} \quad (14)$$

Now one can observe that

$$E_a(f_1(X_{s_1}) \cdots f_n(X_{s_n}))$$

is continuous in  $a$ , if it is considered that

$$\begin{aligned} E_a(f_1(X_{s_1}) \cdots f_n(X_{s_n})) &= \\ &= H_{s_1}(f_1 \cdots (H_{s_{n-1}-s_{n-2}}(f_{n-1} \cdot H_{s_n-s_{n-1}}f_n)) \cdots) \end{aligned}$$

and  $H_s : C \rightarrow C$ .

But  $X_t(\omega)$  being right continuous in  $t$ , one gets

$$f_i(X_{s_i}(\theta_{t+h}\omega)) = f_i(X_{s_i+t+h}(\omega)) \rightarrow f_i(X_{s_i+t}(\omega)) = f_i(X_{s_i}(\theta_t\omega))$$

as  $h \downarrow 0$ .

Now, the equality (13) will result by taking the limit in (14) as  $h \downarrow 0$ .

In this way, for  $G_i$  open in  $S$ , the following equality will result from (13)

$$\begin{aligned} E_a(X_{s_i}(\theta_t\omega) \in G_1, \cdots, X_{s_n}(\theta_t\omega) \in G_n, D) &= \\ &= E_a(P_{X_t}(X_{s_1} \in G_1, \cdots, X_{s_n} \in G_n), D), \end{aligned} \tag{15}$$

and now the Dynkin's theorem can be used.

*Remark 5.* Theorem (Dynkin's formula). Let us suppose that  $\sigma$  is a stopping time with  $E_a(\sigma) < \infty$ . Then, for  $u \in \mathcal{D}(A)$  it follows:

$$E_a \left( \int_0^\infty Au(X_t)dt \right) = E_a(u(X_\sigma)) - u(a).$$

## 5 A problem of financial risk

This section is referred, shortly, to a study of Hu Yaozhong[30] involving the so-called *Onsager-Machlup functional*. This operator is computed for the generalized geometric Brownian motion and also the general equation which the most probable path must satisfy is found. We shall consider only some aspects according to our review G. V. Orman[17].

The most probable path is obtained in a form which permit to conclude about the risk when someone want to invest money into several stocks.

**Definition 3** *The solution of the following stochastic differential equation*

$$dx_t = x_t\{a(t)dw_t + b(t)dt\}, \quad 0 < t < \infty, \tag{16}$$

*is called the **geometric Brownian motion**, where  $a(t), b(t)$  are deterministic functions of  $t$ ;  $w_t$  is a Brownian motion, and  $dw_t$  is the Itô integral.*

Now let us given the following stochastic differential equation

$$\begin{aligned} dx_t &= A(t)x_t dw(t) + B(t)x_t dt \\ x_0 &= \xi \end{aligned} \tag{17}$$

where

$$A(t) = \text{diag} (a_1(t), \dots, a_d(t)) = \begin{pmatrix} a_1(t) & 0 & \dots & 0 \\ 0 & a_2(t) & \dots & 0 \\ \dots & \dots & \dots & \dots \\ 0 & 0 & \dots & a_d(t) \end{pmatrix},$$

$B(t) = (b_{ij}(t))$  satisfying  $b_{ij}(t) \geq 0$  for all  $1 \leq i, j \leq d$ ,  $i \neq j$  and  $w(t) = (w_1(t), \dots, w_d(t))$  are standard Brownian motions which are not necessarily independent.

If  $a_1(t), \dots, a_d(t)$  are continuous functions with bounded derivative one considers

$$B(t) = (b_{ij}(t))_{1 \leq i, j \leq d}$$

where  $b_{ij}(t) \geq 0$ ,  $\forall i \neq j$ .

Denote  $A(t) = \text{diag} (a_1(t), \dots, a_d(t))^T$  and consider the stochastic differential equation

$$\begin{aligned} dx_i(t) &= a_i(t) x_i(t) dw_i(t) + \sum_{j=1}^d b_{ij}(t) x_j(t) dt \\ x_i(0) &= \xi_i \quad i = 1, \dots, d. \end{aligned} \quad (18)$$

Or its integral form

$$x_i(t) = \xi_i + \int_0^t a_i(s) x_i(s) dw_i(s) + \sum_{j=1}^d \int_0^t b_{ij}(s) x_j(s) ds, \quad i = 1, 2, \dots, d. \quad (19)$$

The problem is to perform asymptotic evaluation of the probability

$$P\left\{ \sup_{0 \leq t \leq T} |x(t) - \Phi(t)| < \varepsilon \right\} \quad \text{as } \varepsilon \rightarrow \infty,$$

where  $|\cdot|$  denotes the Euclidian norm in  $d$ -dimensional space, and  $\Phi : [0, T] \rightarrow R$  is a function with continuous and bounded first and second derivatives. [To develop such aspects see, for example, L. Onsager and S. Machlup[15], Y. Takahashi and S. Watanabe[28], O. Zeitouni[31]].

Now we comeback to the geometric Brownian motion. The equation (16) has been successfully applied to the financial problems such as modeling the prices of stocks. For  $i = 1, 2, \dots, d$  we have the stochastic differential equation

$$\begin{aligned} dx_i(t) &= x_i(t) [a_i(t) dw_i(t) + b_i(t) dt] \\ x_i(0) &= \xi_i. \end{aligned} \quad (20)$$

On the other hand, the most probable path  $\Psi_i$  associated to the equation (20) is proved that satisfies the following conditions

$$\begin{aligned} \Psi_i'(t) &= b_i(t) \Psi_i(t) - \frac{1}{2} a_i^2(t) \Psi_i(t), \\ \Psi_i(0) &= \xi_i, \quad i = 1, 2, \dots, d \end{aligned} \quad (21)$$

or, equivalently

$$\begin{aligned}\Psi'_i(t) &= \Psi_i(t) [b_i(t) - \frac{1}{2} a_i^2(t)], \\ \Psi_i(0) &= \xi_i, \quad i = 1, 2, \dots, d.\end{aligned}\tag{22}$$

From this equation we come to the conclusion that if an investment is made in a stock with the mean return  $b(t)$  and the volatility  $a(t)$ , then the real return rate is most likely be given by the equality

$$c(t) = b(t) - \frac{1}{2} a^2(t)\tag{23}$$

instead of  $b(t)$ . That is to say the interest rate is most likely to be  $b(t) - \frac{a^2(t)}{2}$  instead of  $b(t)$ . The quantity  $c(t)$  in (23) is referred to as *the most probable interest rate*.

In conclusion, when an investment is made into several stocks with the mean return  $b_i(t)$  and the volatility  $a_i(t)$  it is recommended to compare the most probable interest rate

$$c_i(t) = b_i(t) - \frac{1}{2} a_i^2(t)$$

instead of the mean interest rate  $b_i(t)$ .

## References

- 1.L. Bachélier. Théorie de la spéculation. Ann. Sci. École Norm. Sup., 17(1900) 21-86.
- 2.A.T. Bharucha-Reid. Elements Of The Theory Of Markov Processes And Their Applications. Dover Publications, Inc., Mineola, New York, 1997.
- 3.G. Da Prato, J. Zabczyk. Stochastic Equations in Infinite Dimensions. Cambridge University Press, 1992.
- 4.G. Da Prato. Stochastic evolution equations by semigroup methods. Quaderns 11, C.R.M., 1998.
- 5.I.I. Gihman, A.V. Skorohod. Stochastic Differential Equations. Spriger-Verlag, Berlin, 1972.
- 6.N. Ikeda, S. Watanabe. Stochastic Differential Equations and Diffusion Processes. 2nd edition, North-Holland, 1989.
- 7.K. Itô. Selected Papers. Springer, 1987.
- 8.K. Itô, H. P. McKean Jr. Diffusion Processes and their Sample Paths. Springer-Verlag Berlin Heidelberg, 1996.
- 9.K. Itô. Stochastic Processes. Eds. Ole E. Barndorff-Nielsen, Ken-iti Sato, Springer, 2004.
- 10.H. J. Kushner, G. G. Yin. Stochastic Approximation Algorithms and Applications. Springer-Verlag New York, Inc., 1997.
- 11.P. Lévy. Processus stochastiques et mouvement brownien. Paris, 1948.
- 12.M. Loève. Probability Theory. Springer-Verlag, New York, 1977.
- 13.B. Øksendal. Stochastic Differential Equations: An Introduction with Applications. Sixth Edition, Springer-Verlag, 2003.
- 14.B. Øksendal, A. Sulem. Applied Stochastic Control of Jump Diffusions. Springer, 2007.

15. ONSAGER, L. MACHLUP, S., *Fluctuations and irreversible processes I, II*, Phys. Rev. 91, 1953, pp. 1505-1512, 1512-1515.
16. G. V. Orman. Chapters of Applied Mathematics (in Romanian). Ed. Alabastră, MicroInformatica, Cluj-Napoca, 1999.
17. G. V. Orman. Review of the paper: Yaozhong, Hu - Multi-dimensional geometric Brownian motions, Onsager-Machlup functions, and applications to mathematical finance. Acta Mathematica Scientia 20B(3):341-358. In: Zentralblatt für Mathematik, Springer-Verlag, Berlin, 2000.
18. G. V. Orman. Lectures on Stochastic Approximation Methods and Related Topics. Preprint, "Gerhard Mercator" University, Duisburg, Germany, 2001.
19. G. V. Orman. On Stochastic Approximation Methods in Reliability. Invited Lecture & Preprint, ICRSA - 2003, University of South Carolina, Columbia, USA, May, 2003.
20. G. V. Orman. Handbook of Limit Theorems and Stochastic Approximation. "Transilvania" University Press, Brasov, 2003.
21. G. V. Orman. On Stochastic Approximation Methods In Systems Analysis. Preprint & Poster, 4ECM, Stockholm, June-July 2004, 12.3, pp. 1-12.
22. G. V. Orman. Techniques of stochastic approximation and some of their applications. A Survey (I). In: G.V. Orman (ed) 21th Scientific Session on MATHEMATICS AND ITS APPLICATIONS, Brasov, pp. 1-12, 2007.
23. G. V. Orman. On Markov Processes: A Survey of the Transition Probabilities and Markov Property. In: Christos H. Skiadas and Ioannis Dimotikalis (eds) Chaotic Systems: Theory and Applications. World Scientific Publishing Co Pte Ltd, pp. 224-231, 2010.
24. G.V. Orman. On a problem of approximation of Markov chains by a solution of a stochastic differential equation. In: Christos H. Skiadas, Ioannis Dimotikalis and Charilaos Skiadas (eds) Chaos Theory: Modeling, Simulation and Applications. World Scientific Publishing Co Pte Ltd, pp. 30-40, 2011.
25. J.M. Steele, Stochastic Calculus and Financial Applications, Springer-Verlag New Yprk, Inc., 2001.
26. Z. Schuss, Theory and Application of Stochastic Differential Equations, John Wiley & Sons, New York, 1980.
27. D. W. Stroock, Markov Processes from K. Itô Perspective, Princeton Univ. Press, Princeton, 2003.
28. TAKAHASHI, Y., WATANABE, S., *The probability functionals (Onsager-Machlup functions) of diffusion processes*, In: Stochastic Integral (Proc. Sympos. Univ. Durham, Durham, 1980). Lect. Notes in Math. 851, 1981, pp. 433-463.
29. M. T. Wasan. Stochastic Approximation. Cambridge University Press, 1969.
30. Hu Yaozhong. Multi-dimensional geometric Brownian motions, Onsager-Machlup functions, and applications to mathematical finance. Acta Mathematica Scientia 20B:341-358, 2000.
31. ZEITOUNI, O., *On the Onsager-Machlup functional of diffusion processes around non- $C_2$  curves*, Ann. Prob., 1989, pp.1037-1054.